OPEN ACCESS



Patchy Kinetic Sunyaev–Zel'dovich Effect with Controlled Reionization History and Morphology

Nianyi Chen 1, Hy Trac 1,2, Suvodip Mukherjee 3, and Renyue Cen 4, McWilliams Center for Cosmology, Department of Physics, Carnegie Mellon University, Pittsburgh, PA 15213, USA; nianyic@andrew.cmu.edu 2 NSF AI Planning Institute for Physics of the Future, Carnegie Mellon University, Pittsburgh, PA 15213, USA 3 Perimeter Institute for Theoretical Physics, 31 Caroline Street N., Waterloo, Ontario, N2L 2Y5, Canada 4 Department of Astrophysical Sciences, Princeton University, Princeton, NJ 08544, USA Received 2022 March 16; revised 2022 July 6; accepted 2022 July 13; published 2023 February 2

Abstract

Using the novel semi-numerical code for reionization AMBER, we model the patchy kinetic Sunyaev–Zel'dovich (kSZ) effect by directly specifying the reionization history with the redshift midpoint $z_{\rm mid}$, duration Δ_z , and asymmetry A_z . We further control the ionizing sources and radiation through the minimum halo mass M_h and the radiation mean free path $\lambda_{\rm mfp}$. AMBER reproduces the free-electron number density and the patchy kSZ power spectrum of radiation–hydrodynamic simulations at the target resolution (1 Mpc h^{-1}) with matched reionization parameters. With a suite of $(2\,{\rm Gpc}/h)^3$ simulations using AMBER, we first constrain the redshift midpoint $6.0 < z_{\rm mid} < 8.9$ using the Planck 2018 Thomson optical depth result (95% CL). Then, assuming $z_{\rm mid} = 8$, we find that the amplitude of $D_{\ell=3000}^{\rm pkSZ}$ scales linearly with the duration of reionization Δ_z and is consistent with the 1σ upper limit from South Pole Telescope (SPT) results up to $\Delta_z < 5.1$ (Δ_z encloses 5%–95% ionization). Moreover, a shorter $\lambda_{\rm mfp}$ can lead to a $\sim 10\%$ lower $D_{\ell=3000}^{\rm pkSZ}$ and a flatter slope in the $D_{\ell=3000}^{\rm pkSZ} - \Delta_z$ scaling relation, thereby affecting the constraints on Δ_z at $\ell=3000$. Allowing $z_{\rm mid}$ and $\lambda_{\rm mfp}$ to vary simultaneously, we get spectra consistent with the SPT result (95% CL) up to $\Delta_z=12.8$ (but $A_z>8$ is needed to ensure the end of reionization before z=5.5). We show that constraints on the asymmetry require $\sim 0.1~\mu$ k^2 measurement accuracy at multipoles other than $\ell=3000$. Finally, we find that the amplitude and shape of the kSZ spectrum are only weakly sensitive to M_h under a fixed reionization history and radiation mean free path.

Unified Astronomy Thesaurus concepts: Cosmic microwave background radiation (322); Sunyaev-Zeldovich effect (1654); Reionization (1383); Cosmology (343)

1. Introduction

The epoch of reionization (EoR) is the period in cosmic history when ionizing radiation emitted by the first galaxies and quasars ionized the baryons in the universe, leading to a transition of the gas content from a neutral state to an ionized state. Because EoR happens at a relatively high redshift $(z = 5 \sim 15)$, the limited observational evidence has hindered our full understanding of the whole physical process involved. Nevertheless, recent and future experiments using various probes are making the picture of the EoR more and more complete. For example, Planck Collaboration et al. (2020) recently inferred $\tau = 0.054 \pm 0.007$ from measurements of the cosmic wave background (CMB) temperature and polarization angular power spectra, implying a late reionization midpoint at redshift $z \approx 7.7 \pm 0.6$ (e.g., Glazer et al. 2018). Becker et al. (2015) find evidence of a dark Ly α trough extending down to $z \approx 5.5$ in the spectrum of a high-redshift quasar, suggesting that reionization could have ended at z < 6 (e.g., Keating et al. 2020), later than previously assumed. In addition, we also expect to gain tomographical information of the EoR through the 21 cm observations, such as the Hydrogen Epoch of Reionization Array (DeBoer et al. 2017) and Square Kilometer Array (Koopmans et al. 2015), and a better understanding of the first ionizing sources through the space-based telescopes

Original content from this work may be used under the terms of the Creative Commons Attribution 4.0 licence. Any further distribution of this work must maintain attribution to the author(s) and the title of the work, journal citation and DOI.

such as the James Webb Space Telescope (Windhorst et al. 2006) and Roman Space Telescope (Spergel et al. 2015).

Of particular interest to this paper is the use of CMB secondary at high multipoles to constrain the EoR. With the improvements in recent ground-based CMB experiments such as the Atacama Cosmology Telescope (ACT⁵) and the South Pole Telescope (SPT^o), we are already able to use anisotropies in the CMB temperature map to constrain reionization through Sunyaev–Zel'dovich (SZ) effect (Zeldovich & Sunyaev 1969; Sunyaev & Zeldovich 1980). The SZ effect results from inverse Compton scattering of CMB photons off high-energy electrons in the intergalactic medium (IGM), and it has the largest contribution among CMB secondary anisotropies on arcminute scales. There are two types of SZ effect: the thermal SZ effect (tSZ) comes from the electron pressure within the intracluster medium and has a spectrum shifted from the CMB blackbody spectrum, while the kinetic SZ (kSZ) effect is due to the bulk motion of electrons in the IGM with respect to the CMB rest frame and has the same spectrum as the CMB (e.g., Carlstrom et al. 2002). The kSZ signal can be further divided into two components that have comparable amplitudes (e.g., Trac et al. 2011; Shaw et al. 2012): a patchy kSZ originates from the inhomogeneous free-electron fraction in the universe during cosmic reionization, and a homogeneous kSZ results from the peculiar velocities of the galaxies after the universe is fully ionized (e.g., Ostriker & Vishniac 1986).

⁵ https://act.princeton.edu

⁶ http://pole.uchicago.edu

Because the patchy kSZ originates from inhomogeneous reionization, its amplitude and power spectrum are sensitive to the timing, duration, and detailed history of reionization. Thus, by probing the patchy kSZ fluctuation we can put constraints on the reionization history provided that we have a thorough understanding of their relation. In recent years, developments in numerical simulations enable us to understand the connection between the patchy kSZ angular power spectrum and reionization (e.g., Zhang et al. 2004; McQuinn et al. 2005; Iliev et al. 2007; Tashiro et al. 2011; Mesinger et al. 2011; Battaglia et al. 2013a; Park et al. 2013; Alvarez 2016; Gorce et al. 2020; Choudhury et al. 2021; Paul et al. 2021). In particular, multiple works have demonstrated that semi-numerical simulations are powerful tools to study kSZ with various reionization scenarios in a relatively quick fashion. For example, Mesinger et al. (2012) and Choudhury et al. (2021) have used semi-numerical simulations to study the dependence of the reionization history and patchy kSZ power spectrum on the ionizing efficiency of high-redshift galaxies, the minimum virial temperature of halos, and the ionizing photon mean free path. Battaglia et al. (2013a) combined N-body simulations with the post-processed reionization-redshift field to study the effect of the reionization history on the patchy kSZ power spectrum. Alvarez (2016) uses very-large-scale simulations to study the different components to the kSZ signal, as well as the four-point statistics of the patchy kSZ.

However, the majority of semi-numerical codes of reionization are based on the excursion set formalism method for reionization (e.g., Bond et al. 1991; Furlanetto et al. 2004), and it has been shown (Zahn et al. 2011) that these semi-numerical methods are in good agreement with radiative-transfer simulations when compared with each other at the same ionization fraction, but not at the same redshift without renormalization. Moreover, most of the semi-analytical models parameterize reionization on the power-spectrum level (e.g., Shaw et al. 2012; Battaglia et al. 2013a; Gorce et al. 2020), without directly controlling the reionization history (but see Paul et al. 2021, who controls the duration of reionization by varying the ionizing efficiency across redshift). This motivates us to study the patchy kSZ signal using the novel semi-numerical simulation Abundance Matching Box for the Epoch of Reionization (AMBER; Trac et al. 2021), which takes the reionization history as direct input.

In this paper, we use the semi-numerical simulation AMBER to generate reionization CMB observables such as the Thomson optical depth and patchy kSZ for different sets of reionization history parameters and cosmological parameters. By doing so, we can disentangle the effect of individual parameters on the observed spectra. We present the dependence of the kSZ power spectrum and Thomson optical depth on the reionization parameters as well as the cosmological parameters.

The paper is organized as follows: In Section 2, we introduce the theory and computation of the Thompson optical depth, the patchy kSZ effect, and the patchy kSZ angular power spectra. In Section 3, we summarize the semi-analytical models used in AMBER, as well as the RadHydro simulations we use to calibrate the AMBER models. Section 4 shows comparisons between the AMBER outputs and the RadHydro simulations with matched reionization parameters and resolutions. In Section 5, we systematically study the effect of the reionization parameters and cosmological parameters on the patchy kSZ signal, including the maps and angular power spectra, and

compare the results with observational constraints. Unless otherwise stated, we assume a flat Λ CDM cosmology with $[\Omega_m, \Omega_b, \sigma_8, n_s, h] = [0.3, 0.045, 0.8, 0.96, 0.7]$, and our fiducial values for the reionization parameters are $[z_{\text{mid}}, \Delta_z, A_z, M_h(M_\odot), \lambda_{\text{mfp}}(\text{Mpc}/h)] = [8.0, 4.0, 3.0, 10^8, 3.0]$ (see later sections for a detailed description of these parameters).

2. Thomson Optical Depth and kSZ Effect

2.1. Thomson Optical Depth

In the ongoing CMB experiment, the most well-constrained EoR observable has been the Thomson scattering optical depth τ_e . Constraints on τ_e inform us about the integrated electron number density n_e along the line of sight, as τ_e is related to n_e by:

$$\tau_e(z, \hat{\boldsymbol{n}}) = \sigma_T \int_0^z dz' \frac{cdt}{dz'} n_e(z', \hat{\boldsymbol{n}}), \tag{1}$$

where σ_T is the Thomson scattering cross section, $\hat{\boldsymbol{n}}$ is the direction of observation, and $n_e(z', \hat{\boldsymbol{n}})$ is the free-electron number density at a specific redshift in the observed direction. The angular variation in τ_e is weak, so we usually drop the angular dependence in the computation and use the global ionization fraction to compute $\tau_e(z)$ instead:

$$\tau_{\rm e}(z) = \sigma_T \int_0^z dz' \frac{cdt}{dz'} \langle n_{\rm e}(z') \rangle_{\rm V}, \qquad (2)$$

where $\langle n_e(z')\rangle_V$ is the volume-averaged free-electron number density.

Because the mean baryon number density increases with the redshift, an earlier reionization leads to higher values of τ_e , and it has been shown that τ_e is not sensitive to the detailed reionization histories beyond the redshift (e.g., Battaglia et al. 2013a). Moreover, current constraints on τ_e are primarily driven by the measurement of the low- ℓ EE polarization power spectrum (which is proportional to τ_e^2) and is independent of the small-scale anisotropies (in particular the patchy kSZ effect). Therefore, constraints on τ_e help break the degeneracy of reionization history parameters in small-scale patchy kSZ measurements. Reversely, one can also use the patchy kSZ signal to break the degeneracy between τ_e and the primordial amplitude of scalar fluctuations A_s (e.g., Alvarez et al. 2021).

2.2. Patchy kSZ Effect

Next, we introduce the patchy kSZ effect and the computation of the kSZ power spectrum. The patchy kSZ effect is the temperature fluctuation in the CMB due to the scattering of CMB photons off of free electrons in bulk motion during cosmic reionization. Small-scale temperature anisotropies are then generated by the coupling of large-scale velocity perturbations and the patchiness of the ionized field on small scales. The fractional temperature fluctuation induced by the patchy kSZ effect is calculated by integrating the electron momentum along the line of sight:

$$\frac{\Delta T_{\text{ksz}}}{T} = \sigma_T \int dz \frac{cdt}{dz} e^{-\tau_e(z,\hat{\boldsymbol{n}})} n_e(z,\hat{\boldsymbol{n}}) \hat{\boldsymbol{n}} \cdot \boldsymbol{v}, \tag{3}$$

where v is the peculiar velocity of free electrons, τ_e is the Thomson optical depth calculated in Equation (1), and the integration limits are the beginning and end of reionization.

Currently, most constraints on reionization from the patchy kSZ come from the angular power spectrum (but see, e.g., Smith & Ferraro 2017, for the use of high-order statistics). This is also the quantity of interest in this paper. To compute the kSZ angular power spectrum, we use the Limber approximation following Park et al. (2013). First, we define the specific free-electron momentum as:

$$q = x_i \mathbf{v}(1+\delta), \tag{4}$$

where x_i is the mass-weighted ionization fraction, ν is the peculiar gas velocity, and δ is the gas overdensity. Then, Equation (3) can be rewritten as:

$$\frac{\Delta T_{\text{ksz}}}{T}(\hat{\boldsymbol{n}}) = \sigma_T n_{e,0} \int_{z_{\text{beg}}}^{z_{\text{end}}} \frac{ds}{a^2} e^{-\tau(z)} \hat{\boldsymbol{n}} \cdot \boldsymbol{q}, \tag{5}$$

where $n_{e,0}$ is the total number of electrons at the present epoch, a is the scale factor, and s is the comoving distance. The kSZ angular power spectrum is given by:

$$C_{\ell} = \left(\frac{\sigma_T n_{e,0}}{c}\right)^2 \int \frac{ds}{s^2 a^4} e^{-2\tau(z)} \frac{P_{q_{\perp}}(k = \ell/s, s)}{2}.$$
 (6)

To compute $P_{q_{\perp}}(k)$, let \tilde{q} be the 3D Fourier transform of the momentum field. Then, the projection of \tilde{q} on the plane perpendicular to the mode vector is given by $\tilde{q}_{\perp}(k) = \tilde{q}(k) - \hat{k}(\tilde{q}(k) \cdot \hat{k})$. Finally, $P_{q_{\perp}}(k)$ is the power spectrum of $\tilde{q}_{\perp}(k)$ given by:

$$(2\pi)^{3}P_{q_{\perp}}(k)\delta(\mathbf{k}-\mathbf{k}') = \langle \tilde{\mathbf{q}}_{\perp}(\mathbf{k}) \cdot \tilde{\mathbf{q}}_{\perp}^{*}(\mathbf{k}) \rangle. \tag{7}$$

Note that we can also directly compute the kSZ power spectrum from full-sky patchy kSZ maps. However, as the scale of interest is small ($\ell > 1000$) and is well-approximated by the Limber approach, we choose to follow the Limber approximation for a less noisy spectrum and faster computation.

3. Simulations

The simulations in this work are run with the new seminumerical code AMBER (Trac et al. 2021). In this section, we will introduce the main models in the AMBER code relevant for calculating the kSZ signal. Moreover, we also briefly introduce the RadHydro simulation suite from the Simulations and Constructions of the Reionization of Cosmic Hydrogen (SCORCH) project (Trac et al. 2015; Doussot et al. 2019; Chen et al. 2020). We will later use these RadHydro simulations to calibrate AMBER models and compare results from both simulations.

3.1. AMBER

3.1.1. Parameterization of the Reionization History

The reionization history $x_i(z)$ is the fraction of hydrogen that is ionized at a certain redshift. It is of primary interest to our understanding of the EoR, because it reveals the possible astrophysical process during the EoR and also directly affects many key EoR observables. For example, the integrated Thomson optical depth and the evolution of the global 21 cm brightness temperature depend linearly on the ionized electron fraction $\bar{x}_i(z)$ and neutral hydrogen fraction $\bar{x}_{H\,I}(z)$, respectively. One of the major novelties of AMBER is that we

directly control the reionization history in our reionization modeling.

Following the argument in Trac et al. (2008), AMBER parameterizes the reionization history with the midpoint, duration, and asymmetry parameters. In AMBER, we use the mass-weighted global ionization fraction $\bar{x}_{i,M}$ and drop the subscript hereafter.

We define the midpoint redshift $z_{\rm mid}$ as the redshift at which 50% of the universe is ionized by mass. To characterize the duration of reionization Δ_z , let $z_{\rm ear} > z_{\rm mid}$ and $z_{\rm lat} < z_{\rm mid}$ correspond to the early and late stages of reionization, respectively. The duration is then defined as:

$$\Delta_{\rm z} \equiv z_{\rm ear} - z_{\rm lat}. \tag{8}$$

There are various definitions of Δ_z in previous works depending on how one defines $z_{\rm ear}$ and $z_{\rm lat}$. Throughout this work, we take ($z_{\rm ear}$, $z_{\rm lat}$) as the redshifts at which the universe is 5% and 95% ionized, respectively. Under this definition, Δ_z more effectively quantifies the whole EoR. We refer to this definition as $\Delta_{z,90}$. We will drop the subscript "90" when we are not explicitly comparing with other definitions of Δ_z . Another popular definition takes ($z_{\rm ear}$, $z_{\rm lat}$) as the redshifts at which the universe is 25% and 75% ionized (e.g., Battaglia et al. 2013b; Gorce et al. 2020). We will refer to the duration under this definition as $\Delta_{z,50}$, as it encloses 50% of the ionization process.

Finally, to characterize the likely asymmetric reionization scenarios, we define the asymmetry parameter as:

$$A_{\rm z} \equiv \frac{z_{\rm ear} - z_{\rm mid}}{z_{\rm mid} - z_{\rm lat}}.$$
 (9)

Symmetric reionization histories would correspond to $A_z=1$, but reionization simulations typically find that the early stage of reionization takes longer than the later stage such that $A_z>1$. Note that with different levels of asymmetry, there is not a one-to-one correspondence between $\Delta_{z,90}$ and $\Delta_{z,50}$. In Figure 1, we show the relation between $\Delta_{z,90}$ and $\Delta_{z,50}$ for asymmetries ranging from 1 to 9. When the asymmetry level is lower, $\Delta_{z,90}$ corresponds to a higher value of $\Delta_{z,50}$. Hence, the scaling coefficient between observables and $\Delta_{z,50}$ is also affected by A_z . This is important for interpreting the comparisons between our results and those of previous works in later sections.

In AMBER, we interpolate the three ionization points at $(z_{ear}, z_{mid}, z_{lat})$ with a modified Weibull function (Weibull 1951),

$$\bar{x}_{i}(z) = \exp\left[-\max\left(\frac{z - a_{w}}{b_{w}}, 0\right)^{c_{w}}\right], \tag{10}$$

where coefficients $a_{\rm w}$, $b_{\rm w}$, $c_{\rm w}$ are all positive values. The coefficients can be easily determined by first solving a nonlinear equation for $c_{\rm w}$ and then substituting its value into algebraic equations for the other two coefficients. We find that solutions exist for the asymmetry range $A_{\rm z} \lesssim 15$, which is more than sufficient for parameter-space studies.

3.1.2. Reionization-redshift Field

The key assumption in AMBER is that the order in which a cell gets ionized is determined by the relative radiation intensity in that cell. In this way, given a global reionization

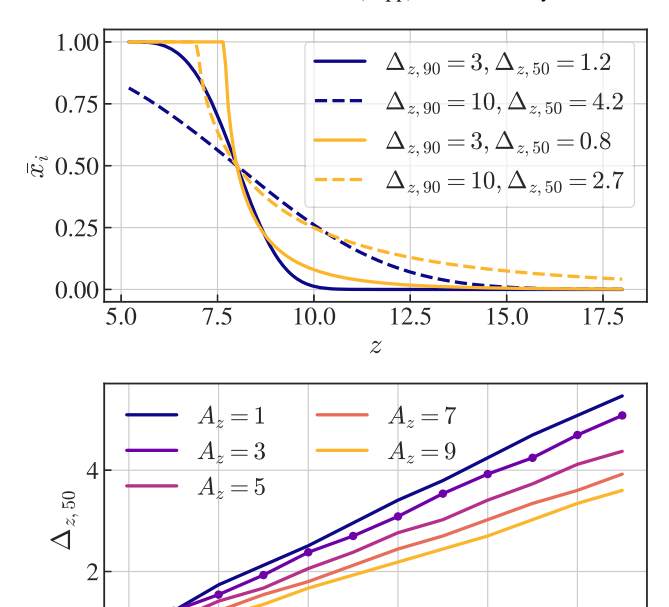


Figure 1. Top: example reionization histories with the same $\Delta_{z,90}$ but different A_z , leading to different $\Delta_{z,50}$. Note that $\Delta_{z,90}$ better captures the high-redshift tail of reionization. Bottom: scaling relation between $\Delta_{z,90}$ and $\Delta_{z,50}$ for different levels of asymmetry.

 $\Delta_{z,90}$

10

12

history $\bar{x}_i(z)$, we can obtain a reionization-redshift field by abundance matching against the unnormalized radiation intensity.

To begin with, the dark matter density and velocity fields are generated with second-order perturbation theory (2LPT) at the desired redshift. On moderately nonlinear scales, the dark matter and gas distributions are highly correlated and assumed to exactly trace each other. Thus we use the dark matter overdensity to approximate the gas overdensity in AMBER.

We then construct halo mass density fields with the Lagrangian version of the excursion set formalism (ESF-L; see Trac et al. 2021, for more detailed descriptions). We use the minimum halo mass parameter M_h to control the lowest halo mass for hosting ionizing sources. This step gives us the halo density field $\rho_{\text{halo}}(x)$, which is a proxy of the ionizing sources in the simulation.

Then, assuming that the radiation intensity of ionizing sources is proportional to the halo density and that the photon flux attenuation follows $e^{-r/\lambda_{\rm mfp}}$, we obtain the (unnormalized) radiation intensity field $r(\mathbf{x}, z)$ by convolving $\rho_{\rm halo}(\mathbf{x})$ with a kernel function $\frac{1}{4\pi r^2} \exp\left(-\frac{r}{\lambda_{\rm mfp}}\right)$. $\lambda_{\rm mfp}$ would affect how much radiation is received by each cell in our simulation, and as a result how early each cell is ionized. Here we use an effective mean free path $\lambda_{\rm mfp}$ to account for the attenuation of the radiation field. In principle, the mean free path of photons is a local variable that could depend on the halo mass and redshift. However, given the semi-analytical nature of our model and the

resolution at 1 Mpc h^{-1} , we set the photon mean free path as a global variable $\lambda_{\rm mfp}$. We plan to incorporate the temporal and spatial variations of $\lambda_{\rm mfp}$ in future developments.

Finally, the reionization-redshift field $z_{\rm re}(x)$ is assumed to be correlated with the radiation field r(x, z). A region with higher radiation intensity is considered to be photoionized earlier and has a higher. The abundance matching technique assigns redshift values such that the reionization history follows a given mass-weighted ionization fraction $\bar{x}_i(z)$, specified with the redshift midpoint, duration, and asymmetry parameters and interpolated with a Weibull function (Equation (10)).

We perform the abundance matching based on the radiation field at a single redshift z_{mid} for computational efficiency, but it can also be done tomographically using multiple redshift intervals. In the Appendix, we discuss the effect of abundance matching at a single redshift z_{mid} and characterize the changes in the electron number density as well as the patchy kSZ signal when the abundance matching redshift is chosen differently. The abundance matching at z_{mid} is performed as follows: at a given redshift bin z_n , we have a corresponding mass-weighted ionization fraction $\bar{x}_i(z_n)$ from the specified reionization history. We then rank the cells at this redshift in descending order by $r(x, z_{mid})$. Then we ionize the first k_n cells by this rank so that we reach an ionized mass fraction of $\bar{x}_i(z_n)$. Here the ionized mass fraction is calculated from the linearly extrapolated overdensity with respect to the overdensity at the midpoint redshift. We note that the volume-weighted ionization fraction in this case is k_n/N_{cell} , and it is typically lower than the mass-weighted $\bar{x}_i(z_n)$.

3.2. RadHydro

The SCORCH project (Trac et al. 2015; Doussot et al. 2019; Chen et al. 2020) is a set of *N*-body and radiation–hydrodynamic simulations that is designed to provide theoretical predictions and mock observations of reionization for more accurate comparisons with present and future observations. It is the motivation of AMBER, so we will briefly summarize the SCORCH simulations here. For details of the SCORCH project, please refer to Trac et al. (2015) and Doussot et al. (2019).

SCORCH II (Doussot et al. 2019) is a set of three radiation-hydrodynamic (RadHydro) simulations with the same cosmic initial conditions, same galaxy luminosity functions, but different radiation escape fraction $f_{\rm esc}(z)$ models. The simulations are designed to have the same Thomson optical depth $\tau \approx 0.06$, consistent with recent CMB observations (Planck Collaboration et al. 2020), and similar midpoints of reionization $7.5 \lesssim z \lesssim 8$, but different evolution of the ionization fraction $\bar{x}_i(z)$. They model high-redshift galaxies using an updated subgrid approach that allows systematic control of the galaxy distributions in the simulations while matching the observed luminosity functions from the Hubble Space Telescope (e.g., Bouwens et al. 2015; Finkelstein et al. 2015).

Table 1 summarizes the parameters for RadHydro Sim 1, which we will later use to compare with the output of AMBER. Here a_8 and f_8 define the redshift dependence of the photon

 Table 1

 Simulation Parameters and Measured Reionization History Parameters for RadHydro Sim 1 in SCORCH II

Model	$L(h^{-1}\mathrm{Mpc})$	$N_{ m dm}$	$N_{ m gas}$	$N_{ m RT}$	f_8	a_8	au	$z_{ m mid}$	Δ_{z}	A_{z}	$M_{ m h}$
Sim 1	50	2048 ³	2048 ³	512 ³	0.13	1	0.060	7.91	5.45	2.69	$10^8 M_{\odot}$

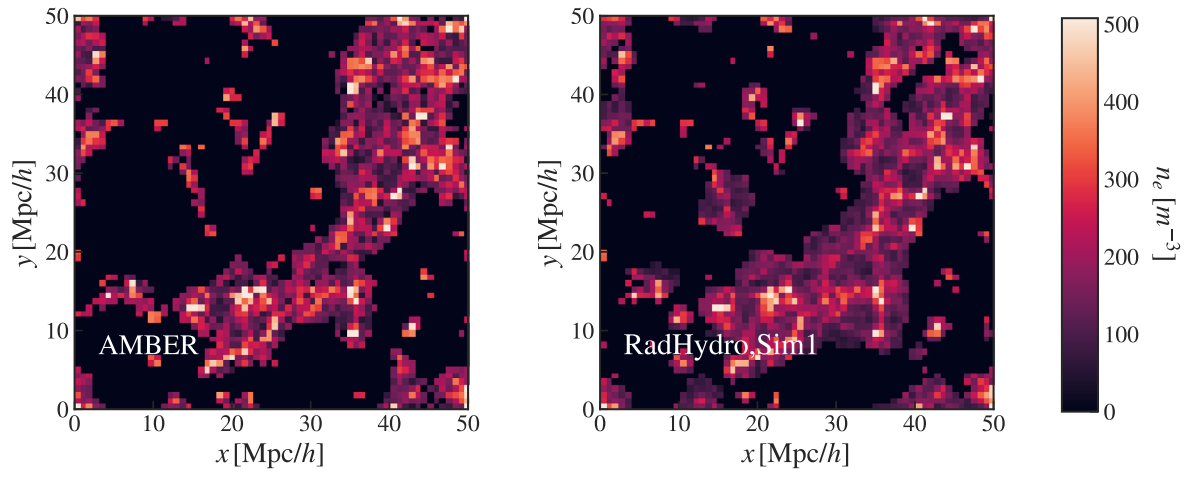


Figure 2. Visualization of a 50 Mpc $h^{-1} \times 50$ Mpc $h^{-1} \times 1$ Mpc h^{-1} (shown in 64² pixels) slice of the free-electron number density at z = 8 from RadHydro Sim 1 and AMBER with matched reionization parameters. AMBER produces slightly more concentrated ionized regions compared to RadHydro.

escape fraction through $f_{\rm esc}(z)=f_8\Big(\frac{1+z}{9}\Big)^{a_8}$ (see Doussot et al. 2019 for a more detailed description). We also show the measured midpoint, duration, and asymmetry parameters from the simulation output.

4. Comparison with RadHydro

In this section, we present the comparison of the freeelectron number density, the patchy kSZ 2D projected maps, and the patchy kSZ power spectra between AMBER and RadHydro Sim 1.

As our target resolution when running AMBER is 1 Mpc h^{-1} , we first bin down the RadHydro Sim 1 to 64^3 cells in the 50 Mpc h^{-1} box. More specifically, for the density and momentum fields we take the average over a 83 local region, and for the reionization-redshift field, we smoothed it by calculating the redshift at which all 8³ local cells are ionized. Then we remeasure the reionization parameters in the binned Sim 1 and obtain $z_{\text{mid}} = 7.85$, $\Delta_z = 4.73$, $A_z = 2.25$. Note that this is slightly different from the parameter measured in the original resolution shown in Table 1 because we have averaged over a much larger region when determining the reionization redshift. In particular, some cells with early reionization may be postponed to a later time because the surroundings are not yet ionized. For the comparison, we run AMBER at the same resolution (64³), with the same cosmological parameters and the same initial condition phase as RadHydro Sim 1, and we match the reionization parameters measured above. In RadHydro Sim 1, the minimum halo mass is $10^8\,M_\odot$, so we fix this parameter in AMBER. By varying $\lambda_{\rm mfp}$ in the range [1 Mpc/h, 5 Mpc/h], we find that $\lambda_{\rm mfp} = 2.8$ Mpc h^{-1} best matches the reionization-redshift field of RadHydro Sim 1, so we present our comparison results at this value. Because we use a small box here, we can calculate the maps under the flat-sky approximation and do the 2D projection by summing the field along the z-axis at a fixed redshift.

4.1. Free-electron Number Density

We first examine the evolution of the free-electron number density, as it is a crucial component for calculating both the Thomson optical depth and the patchy kSZ signal. The fluctuation in the free-electron number density will dominate the patchy kSZ signal on small scales.

After getting the reionization-redshift field z_{re} following the procedures described in Section 3.1, we can use it to obtain the electron number density field at all redshifts by

$$n_e(\mathbf{x}, z) = x_i(\mathbf{x}, z) n_b(\mathbf{x}, z) \left(X + \frac{Y}{4} \right), \tag{11}$$

where n_b is the baryon number density, X is the mass fraction of hydrogen, Y is the mass fraction of helium. $x_i = n_{\text{e,free}}/n_{\text{e,total}}$ is the free-electron fraction, and is set to $x_i(\mathbf{x}, z) = 1$ if $z < z_{re}(\mathbf{x})$ and $x_i(\mathbf{x}, z) = 0$ if $z > z_{re}(\mathbf{x})$.

In Figure 2 we show the visualization of a $50 \times 50 \times 1 \,\mathrm{Mpc}^3 \,h^{-3}$ slice of the free-electron number density at z=8 from RadHydro Sim 1 and AMBER with matched reionization parameters. At z=8, about half of the mass in the universe is ionized, and we can see from both simulations that the ionized regions also correspond to the higher-density regions. The morphology of the ionized regions from the AMBER code is very similar to that from RadHydro Sim 1. However, from the slice we notice that the RadHydro simulation has a larger ionized region in volume. Given the same mass-weighted ionization fraction, a larger volume filling factor in RadHydro means that the mean density of the ionized region is smaller and that the ionizing front propagates further into the IGM.

This is confirmed by the distribution of the gas density in the ionized regions shown in Figure 3. We can see from the distribution that the ionized regions in AMBER have a peak at higher densities compared to those in RadHydro, especially during the early stage of reionization ($\bar{x}_i < 0.5$). This happens for two main reasons. First, the high-density regions have a high recombination rate and may remain neutral in RadHydro. However, this is currently not treated in AMBER, and thus AMBER tends to ionize more high-density regions. Second, the RadHydro simulations have episodic star formation, and the highest-density collapsed regions do not necessarily produce the highest number of photons. These fluctuations show up more when there are small HII regions early on during reionization. The two processes combined lead to the more tilted probability density function (PDF) of the ionized gas density in AMBER.

Then in Figure 4, we further compare between the AMBER and RadHydro free-electron number density power spectra $P_{ee}(k, z)$ at different ionization levels. In both simulations, the

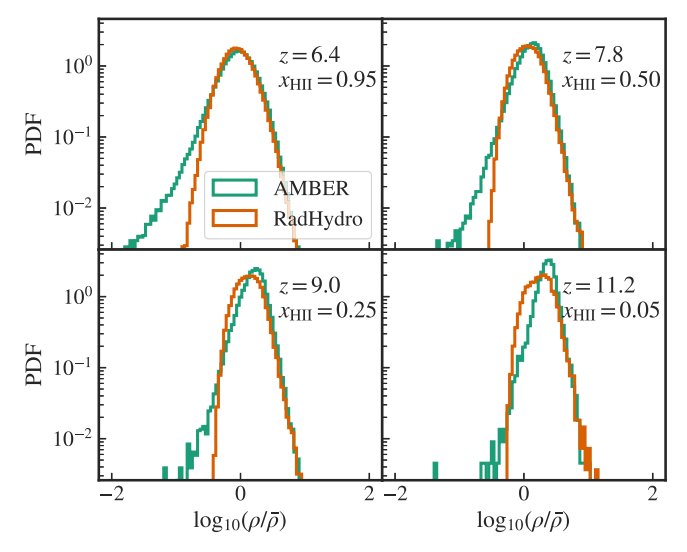


Figure 3. Distribution of gas densities in ionized regions. The ionized regions in AMBER have a peak at higher densities compared to RadHydro, especially during the early stage of reionization ($\bar{x}_i < 0.5$). The disagreement in underdense regions is not concerning because it is due to the much smaller number of LPT particles and the different assignment and deconvolution process for AMBER. We would find the same effects for RadHydro if we used a lower-resolution simulation and had not performed simple binning.

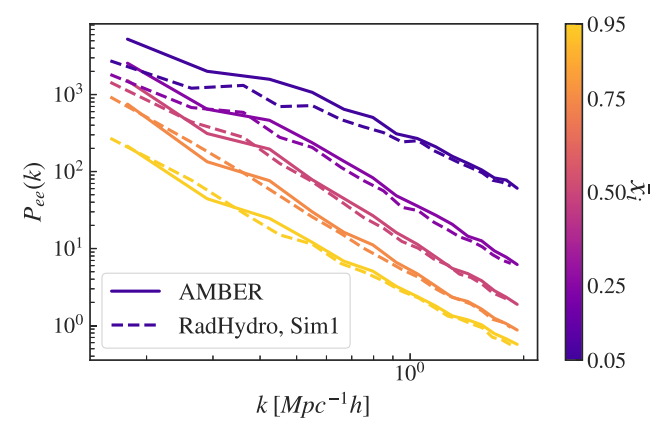


Figure 4. Comparison between the AMBER and RadHydro free-electron number density power spectrum $P_{ee}(k,z)$ at different redshifts. In both simulations, the overall $P_{ee}(k,z)$ gets lower as reionization evolves, because as more mass in low-density regions get ionized, the ionized electron field becomes a less biased tracer of the matter density field. At very high redshift, AMBER has larger power on large scales, but from z=9 onward, the two simulations match well with each other.

overall $P_{ee}(k, z)$ gets lower as reionization evolves, because as more mass in low-density regions gets ionized, the ionized electron field becomes a less biased tracer of the matter density field. At the beginning of reionization, the ionized regions are concentrated in high-density regions around the source galaxies, and therefore n_e has a higher power on large scales compared to the underlying matter density field. From the comparison between the two simulations, we see that when reionization just begins ($z \sim 12$), AMBER has larger power on large scales. The disagreement in underdense regions is not concerning because it is due to the much smaller number of LPT particles and the different assignment and deconvolution process for AMBER. We would find the same effects for RadHydro if we used a lower-resolution simulation and had not performed simple binning. As we have already seen in Figure 3, AMBER ionizes more high-density regions during

the beginning of reionization. This leads to more bias on large scales at high redshifts.

From z = 9 onward, the two simulation match well with each other, because the bias in AMBER is less prominent as the ionizing fronts propagate further into the low-density regions. Finally, once reionization is almost over ($z \sim 6$) and all IGM atoms are ionized, the fluctuations in the free-electron density follow those of dark matter on large scales.

4.2. Patchy kSZ

Next, we compare the 2D projected patchy kSZ temperature maps under the flat-sky approximation for RadHydro and AMBER. To get the flat-sky maps, we simply sum the free-electron momentum along the *z*-axis to get the fractional temperature difference in the CMB introduced by the patchy kSZ effect, and then multiply by the CMB temperature $T_{\rm CMB} = 2.725 {\rm k}$ to obtain the temperature fluctuation in the 2D plane. Here we assume a fixed $z = z_{\rm mid}$ ($x_{\rm H\ II} = 0.5$) as the box size is small enough for ignoring the redshift evolution.

From the projected maps in Figure 5, we can see that visually the AMBER kSZ signal resembles that of RadHydro Sim 1. The blue and red regions correspond to the signal from the ionized regions along the line of sight, while the small white regions are neutral. Similar to what we have seen in Figure 2, because RadHydro has larger ionized regions, we see fewer white pixels in the kSZ map here.

Besides the visualization, in Figure 6 we further show the one-point and two-point statistics for the projected kSZ maps. The distributions of the temperature fluctuations shown in the top panel are very similar in the two simulations. From the PDF we do see a higher peak around $\Delta T = 0$ from AMBER, as we have discussed from the maps in the previous paragraph. Other than the difference in the peak, the overall shape and width of the distribution match well.

The bottom panel shows the dimensionless power spectrum of the flat-sky maps, related to the angular power spectrum C_{ℓ} by $D_{\ell} = \ell(\ell+1)C_{\ell}/2\pi$. We first notice that from both simulations, the power spectrum peaks at $\ell \sim 3500$. This scale corresponds to a size of the ionized bubbles of $\sim 11 \,\mathrm{Mpc}\,\mathrm{h}^{-1}$ at z = 7.8. Then, comparing the two curves, we see that the spectrum of RadHydro has ~5% higher power on small and large scales, while AMBER produces ~10% higher power at ℓ = 3500–4000. There are two sources of the differences: first, RadHydro uses a P^3M N-body simulation to generate the velocity field, while AMBER uses 2LPT and produces less power on small scales compared to N-body simulations (see, e.g., Trac et al. 2021); second, as was shown in the previous section, there are also differences in the free-electron number density field due to the slightly different morphology of ionized regions. To disentangle the two effects, we also show the spectrum calculated using the AMBER n_e field with the velocity from RadHydro (shown in dashed purple). We can see that, when we correct for the difference from the velocity fields, the power on small scales ($\ell > 6000$) matches perfectly with RadHydro. This indicates that the small-scale difference is primarily due to the coupling of the n_e fields with the velocity fluctuations. For $\ell < 6000$ multipoles, however, using the RadHydro velocity does not change the kSZ spectrum in AMBER. This tells us that $\ell < 6000$ arises from the difference in the free-electron number density. Despite the minor differences we just discussed, we still find that overall the

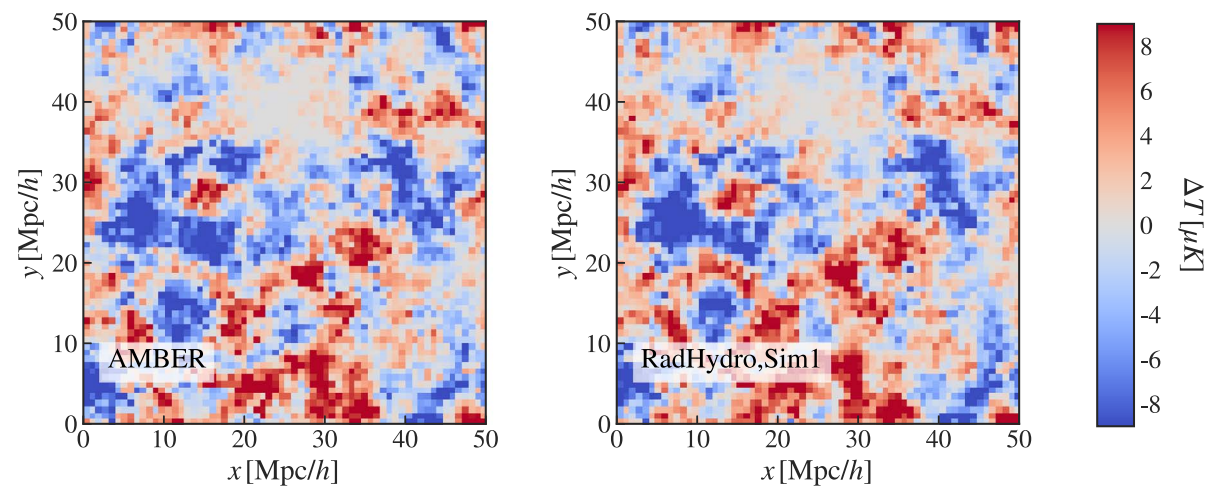


Figure 5. 2D projected patchy kSZ temperature maps under the flat-sky approximation for RadHydro Sim 1 (right) and AMBER (left) in the same simulation as described in Figure 2. The projection is done at redshift z = 8.0. Here we sum the electron momentum along the z-axis to get the fractional temperature difference in the CMB. The projected kSZ map of AMBER resembles that of RadHydro Sim 1 when the reionization parameters are matched.

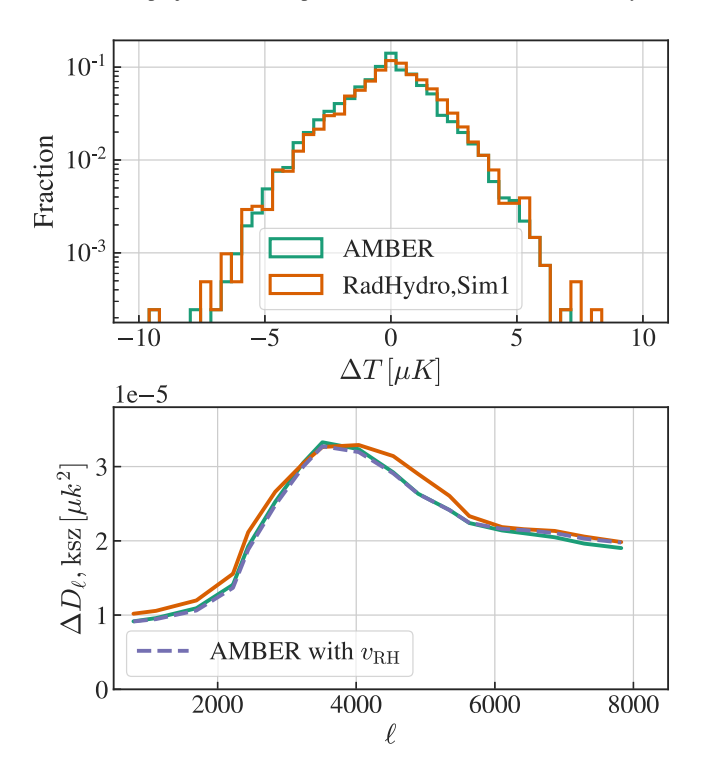


Figure 6. Top: distribution of ΔT of the projected kSZ maps generated using AMBER (green) and RadHydro (orange) shown in Figure 5. Bottom: 2D power spectra of the patchy kSZ maps from the two simulations. To disentangle the effect from the velocity difference, we also show the spectrum calculated using the AMBER n_e field with the velocity from RadHydro (dashed purple). We find good agreement at $\ell \sim 3000$. The difference at $\ell < 6000$ mainly results from the electron number density as opposed to the velocity.

kSZ 2D spectrum from AMBER matches well with that from RadHydro.

5. Parameter-space Study

Having shown that AMBER agrees well with the RadHydro simulation for observations at the matched parameter values, now we vary the parameters around their fiducial values in order to study their effect on the patchy kSZ signal. We summarize the fiducial values for the parameters we study in Table 2. Previous works (e.g., Zahn et al. 2007, 2012;

Mesinger et al. 2012; Battaglia et al. 2013a) have shown that the kSZ signal from patchy reionization depends on the midpoint redshift and duration of reionization. However, they did not directly parameterize the simulations with these parameters, so it is hard to control the reionization history and directly study its influence on the patchy kSZ signal. In this work, we will directly examine the effect of the reionization history, parameterized by the midpoint, duration, and asymmetry, on the patchy kSZ effect of reionization. To generate the kSZ maps and power spectra shown in this section, we run $L_{\text{hox}} = 2 \,\text{Gpc}/h \,\text{simulations on } 2048^3 \,\text{grids.}$

5.1. Redshift Midpoint

The midpoint redshift $z_{\rm mid}$ is the redshift at which half of the universe is ionized (by mass). When other parameters are kept fixed, a higher $z_{\rm mid}$ means that the whole reionization process is pushed to an earlier time when the universe has a higher energy density. We note that, because we currently generate the reionization-redshift field by abundance matching at $z_{\rm mid}$, a change in $z_{\rm mid}$ can also affect the relative order of ionization of the cells (i.e., we do not preserve the exact same ionization morphology by fixing all other parameters). However, we expect such an effect to be small, because the large halos at z=9 should also correspond to large halos at z=7. Therefore, we expect the main effect from varying $z_{\rm mid}$ to be the amplitude of the kSZ spectra: the overall amplitude should be larger with a higher $z_{\rm mid}$, because there would be a higher electron density when we integrate along the line of sight.

In the top two panels of Figure 7, we visualize the free-electron number density n_e and the kSZ temperature change $\Delta T_{\rm kSZ}$ for relatively early $(z_{\rm mid}=9)$ and late $(z_{\rm mid}=7)$ reionization. In this figure, the horizontal axis is the line of sight, and in the direction perpendicular to the page we plot a 1 Mpc h^{-1} slice from the 3D simulation box. From the n_e plots, we can see that ionized bubbles form around the first galaxies at the beginning of reionization. These bubbles continue to grow in size and finally overlap and merge, leading to a fully ionized universe. In the left panel of Figure 10, we can see that increasing the midpoint redshift of reionization increases the amplitude of the kSZ spectra without changing the shape. Physically, the scenario that corresponds to an earlier $z_{\rm mid}$

 Table 2

 Fiducial Parameters for the Parameter-space Study using AMBER

$L(h^{-1}\text{Mpc})$	$N_{ m grid}$	Ω_m	σ_8	z_{mid}	Δ_{z}	$A_{\rm z}$	$M_{ m h}$	λ_{mfp}
2000	2048 ³	0.3	0.8	8.0	4.0	3.0	10^8M_\odot	$3.0 {\rm Mpc}h^{-1}$

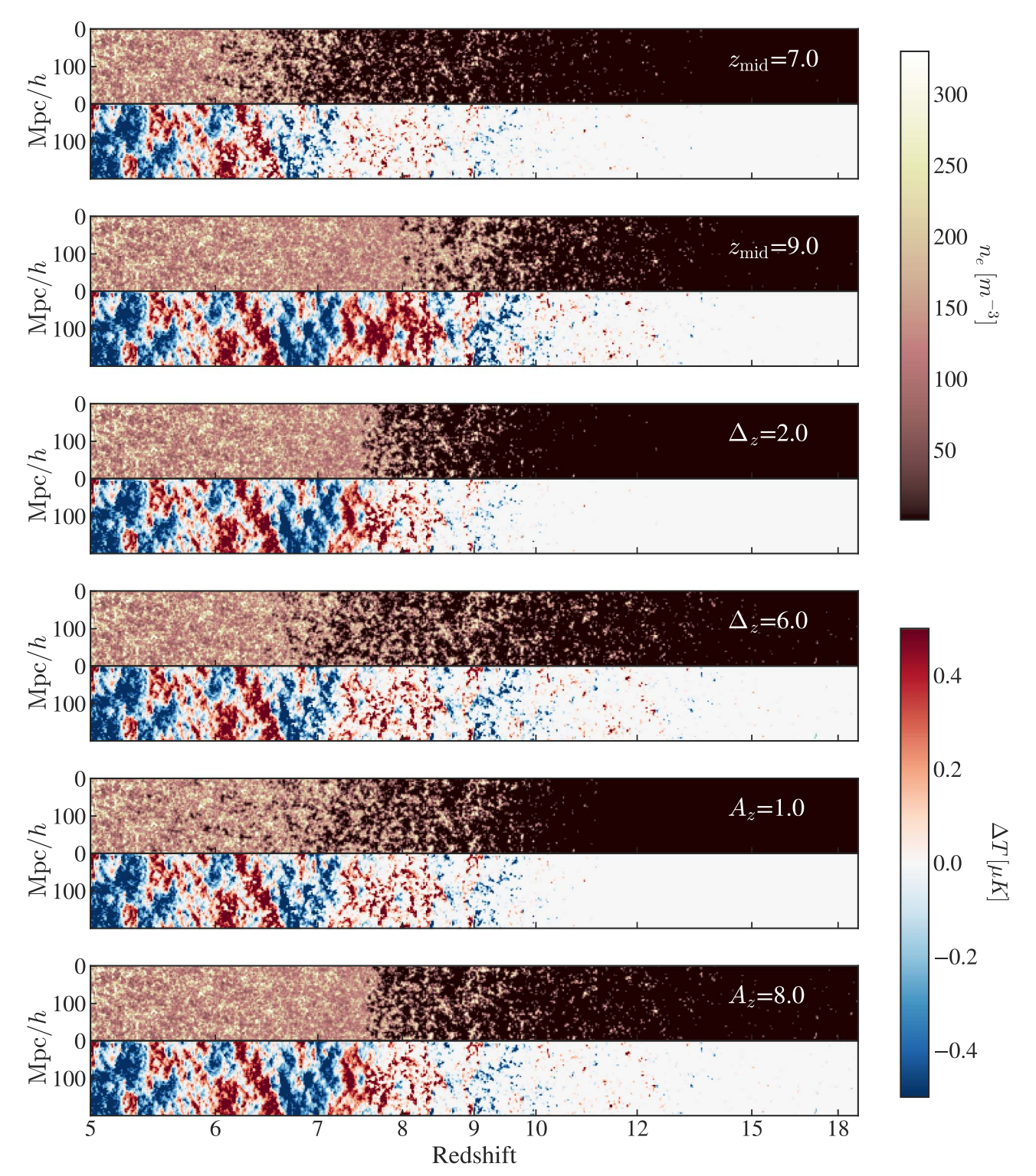


Figure 7. Visualization of the redshift evolution of n_e (dark background) and $\Delta T_{\rm kSZ}$ (white background). Rows 1/2: We vary the midpoint of reionization from $z_{\rm mid}=7.0$ to $z_{\rm mid}=9.0$ while keeping other parameters at their fiducial values. Rows 3/4: We vary the duration of reionization from $\Delta_z=2.0$ to $\Delta_z=6.0$. We can see the large-scale velocity coherence across redshifts. With a longer duration, there are more ionizing bubbles stacked along the line of sight. Rows 5/6: We vary the asymmetry of the reionization history from $A_z=1.0$ to $A_z=8.0$. With a larger A_z , ionizing bubbles begin to form as early as z=18, although $z_{\rm mid}$ and Δ_z are kept fixed.

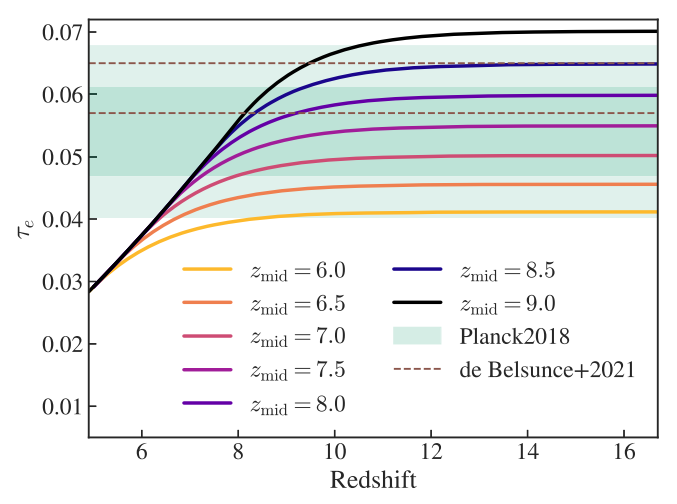


Figure 8. Evolution of τ_e with different values of $z_{\rm mid}$ ranging from $z_{\rm mid} = 6.0$ to $z_{\rm mid} = 9.0$. Out of the values shown, $z_{\rm mid} = 9.0$ is mildly inconsistent with the constraint from Planck Collaboration et al. (2020) at the 2σ level, while the other values are consistent. The dashed band shows the reanalysis of the Plank 2018 data by de Belsunce et al. (2021), who found larger values of τ_e and favor a higher $z_{\rm mid}$.

could be a higher escape fraction, ionization dominated by smaller sources, or a combination of multiple effects.

We note that there exist degeneracies between z_{mid} and other reionization parameters (most noticeably the duration of reionization), in terms of their effects on the patchy kSZ power spectrum (we will discuss more about it later). Such degeneracy is often broken by constraints from the Thompson optical depth τ_e from the low- ℓ EE polarization (e.g., Ferraro & Smith 2018). The value of τ_e is mainly affected by the redshift of reionization without being sensitive to other reionization parameters (e.g., Battaglia et al. 2013a). In Figure 8, we show the evolution of τ_e with different values of z_{mid} ranging from $z_{\rm mid} = 6.0$ to $z_{\rm mid} = 9.0$. Out of the values shown, $z_{\rm mid} = 9.0$ is mildly inconsistent with the constraint from Planck Collaboration et al. (2020), while the other values are all within the 2σ range. However, we note that recent reanalysis of the Planck 2018 data by Pagano et al. (2020) and de Belsunce et al. (2021; shown as dashed lines) found larger values of τ_e and favors higher z_{mid} . In either case, the constraint we get from τ_e on z_{mid} is tighter compared to the constraint from the purely patchy kSZ.

5.2. Duration

In the previous section, we have hinted at the degeneracy between z_{mid} and the duration of reionization. Now we will turn to the effect of the duration on the patchy kSZ temperature fluctuations. Out of all the reionization parameters, Δ_z has the strongest effect on the amplitude of the spectra. For this reason, observations of the kSZ amplitude have been used to constrain the reionization duration for the past decade. The ACT and SPT-SZ surveys have published upper limits on the kSZ power (Addison et al. 2013; Dunkley et al. 2013; George et al. 2015), with a 95% CL upper limit on the patchy kSZ power being $D_{\ell=3000}^{\mathrm{pkSZ}} < 3.3 \mu\mathrm{K}^2$ from the 2500 degree² SPT-SZ survey. By combining SPT results with large-scale CMB polarization measurements, Zahn et al. (2012) constrain the amplitude of the patchy kSZ by setting an upper limit $D_{\ell=3000}^{\rm pkSZ} \leqslant 2.1 \mu {\rm K}^2$ (95% CL). The most recent observational constraints come from the SPTPol survey, where Reichardt et al. (2021) constrained the patchy kSZ amplitude to $D_{\ell=3000}^{\rm pkSZ}=1.1^{+1.0}_{-0.7}\mu{\rm K}^2$ using the models of homogeneous signal given in Shaw et al. (2012). Using the fitting template provided in Battaglia et al. (2013a), they find the 95% CL upper limits on the duration of reionization to be $\Delta_{z,50} < 5.4$ (6.9/4.3 when considering a 25% uncertainty in the homogeneous spectrum), and a 68% confidence interval of $\Delta_{z,50} = 1.1^{+1.6}_{-0.7}$. Using a more recent semi-numerical model, Choudhury et al. (2021) placed a tighter constraint on the duration to be $\Delta_{z,50}$ < 2.9 at 99% CL.

Before diving into the kSZ angular power spectra prediction with AMBER, we start by visualizing the patchy kSZ temperature fluctuations with different durations of reionization. In the middle panels of Figure 7, we show the light-cone projections of the free-electron number density n_e and the kSZ temperature change $\Delta T_{\rm kSZ}$ assuming a quick reionization $(\Delta z = 2$, third row) and a slow reionization ($\Delta z = 6$, fourth row). From the comparison between the two durations, we see that under the $\Delta z = 6$ scenario, reionization starts earlier, and there are more ionized bubbles along the line of sight. The motion of these ionized bubbles relative to the background CMB would result in the observed kSZ fluctuation in the CMB we see from the bottom panels. In the bottom panels, we can clearly see the large-scale velocity fluctuations. These fluctuations dominate $\Delta T_{\rm kSZ}$ on large scales, while the n_e field fluctuations dominate on small scales.

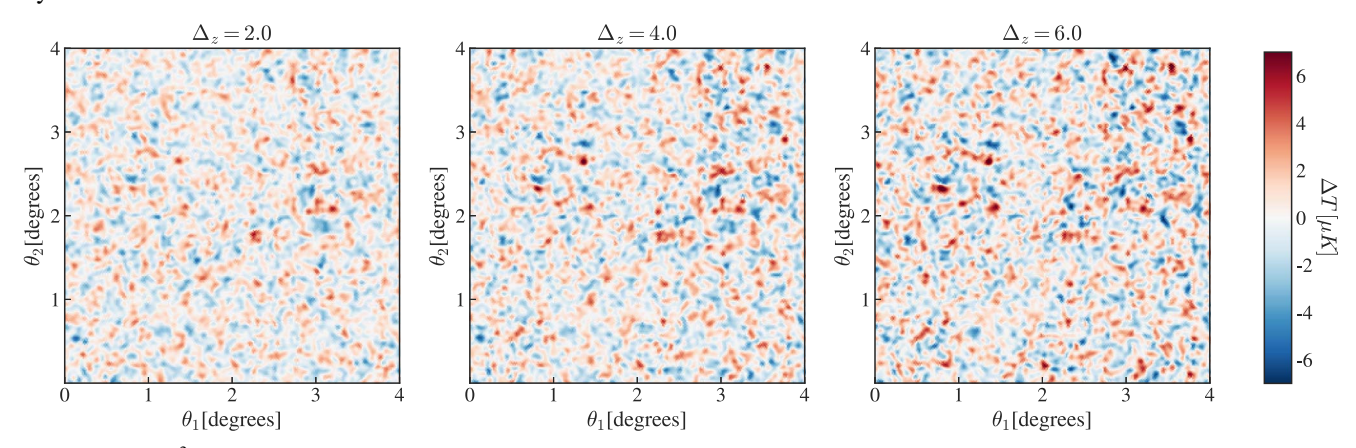


Figure 9. 4×4 degree² maps of the kSZ temperature fluctuation for different durations of reionization. This is a filtered map with only the small-scale ($\ell > 1000$) modes to show the effect of patchy reionization rather than the large-scale velocity fluctuation. A longer duration ($\Delta_z = 6$, right) leads to larger fluctuations on small scales, while the map with a shorter duration appears to be smoother. This is because the small-scale kSZ is sourced by the electron number density fluctuation from patchy reionization. These fluctuations are incoherent and accumulate along the line of sight, leading to a larger small-scale inhomogeneity for a longer duration.

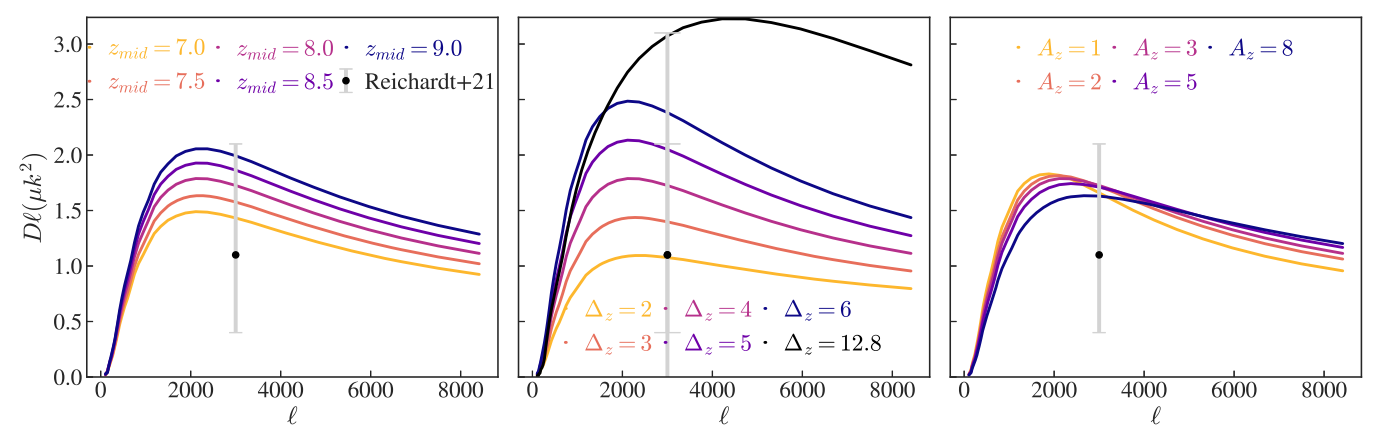


Figure 10. Patchy kSZ angular power spectrum for different reionization history parameters. The fiducial parameters are $[z_{\rm mid}, \Delta_z, A_z] = [8.0, 4.0, 3.0]$. The smaller error bars show the 1σ confidence interval of $D_{\ell=3000}^{\rm kSZ}$ from Reichardt et al. (2021), and the larger error bar in the middle panel shows the 2σ confidence interval. Left: The overall amplitude of the kSZ spectrum increases as we shift the midpoint redshift of reionization earlier, but all variations are consistent with the 1σ interval. Middle: Increasing the duration of reionization also increases the overall power of the kSZ spectrum, and it affects the kSZ amplitude most significantly. The black line shows the maximum Δ_z that produces $D_{\ell=3000}^{\rm kSZ}$ within the 2σ interval, where we let $z_{\rm mid}=6.5$, $A_z=8$ (to ensure reionization ended before z=5.5), and $\lambda_{\rm mfp}=1.0$ Mpc h^{-1} . Right: The asymmetry parameter A_z does not have a big impact on the kSZ spectrum comparing with the midpoint and duration, but we can see that increasing the asymmetry (meaning that the beginning of reionization is longer) results in a flatter slope of the kSZ spectrum.

In Figure 9, we show 4×4 degree² patches of the $\Delta T_{\rm kSZ}$ maps from the $2\,{\rm Gpc}/h$ simulations with different durations. These maps are made by ray tracing through past light cones during reionization ($5\leqslant z\leqslant 30$) and are generated using HEALPix (Górski et al. 2005) with $N_{\rm side}=4\times N_{\rm mesh}$. The maps shown here are processed with a high-pass filter, where we only keep the spherical harmonics with $\ell>1000$. This is because we are more interested in the small-scale features, which are a direct result of patchy reionization. From the maps, we can see that a longer duration leads to larger fluctuations on small scales, because the small-scale kSZ is sourced by the electron number density fluctuation from patchy reionization. These fluctuations are incoherent and accumulate along the line of sight, leading to a larger small-scale inhomogeneity for a longer duration.

Finally, we show the change in the angular power spectra with respect to the duration in the second panel of Figure 10. Compared with the first panel on z_{mid} , we see a strong degeneracy of the two parameters as expected, but the spectra are more sensitive to the duration than the midpoint redshift. Here we also show the 1σ and 2σ confidence intervals derived in Reichardt et al. (2021), in order to show the extent of variation with the Δz parameter within the confidence intervals. For the colored lines, we keep all other parameters at their fiducial values, and we can see that durations of $\Delta_z < 5.1$ yield results consistent with the 1σ constraints from Reichardt et al. (2021). This translates to $\Delta_{z,50}$ < 2.0 under the definition of duration in Battaglia et al. (2013b), assuming a mildly asymmetric reionization history at $A_z = 3$ (see Figure 1 for the conversion). The limit agrees with the recent picture from a variety of observations arguing that reionization happened quickly.

Then we explore the maximum Δ_z that produces a $D_{\ell=3000}^{\rm pkSZ}$ consistent with the 2σ constraint from Reichardt et al. (2021). In order to do this, we also vary the other two parameters, $z_{\rm mid}$ and $\lambda_{\rm mfp}$, that affect $D_{\ell=3000}^{\rm pkSZ}$ most. As we know that lower values of $z_{\rm mid}$ and $\lambda_{\rm mfp}$ decrease $D_{\ell=3000}^{\rm pkSZ}$, we want $z_{\rm mid}$ and $\lambda_{\rm mfp}$ to be low in order to allow for a longer duration. We set $z_{\rm mid}=6.5$, a value slightly below the 1σ interval from the τ_e prediction from Planck Collaboration et al. (2020). We also set $\lambda_{\rm mfp}=1~{\rm Mpc}~h^{-1}$ and $A_z=8.0$ in order to ensure an end of

reionization by z=5.5. After minimizing $D_{\ell=3000}^{\text{pkSZ}}$ with other parameters consistent with other observation channels, we find that a duration of $\Delta_z=12.8$ reaches the top of the 2σ interval. This converts to $\Delta_{z,50}<3.5$ under the assumption that $A_z=8.0$.

We emphasize, however, that this should not be interpreted as a strict 2σ constraint of $\Delta_z < 12.8$ (or $\Delta_{z,50} < 3.5$), because here we do not systematically vary other reionization parameters. A full parameter-space study is needed in order to derive a constraint on the duration from the simulation data and the observation data. We also note that our D_ℓ^{pkSZ} are integrated from z=5 to z=30, while the confidence interval given in Reichardt et al. (2021) is derived using an end-of-reionization redshift of z=5.5. Converting to an end-of-reionization redshift of 5.0 may move the interval up by $\sim 5\%$ – 10%. Finally, the uncertainty within the homogeneous kSZ spectra can cause $\sim 25\%$ fluctuations in the patchy kSZ estimation, according to Reichardt et al. (2021).

5.3. Asymmetry

The asymmetry parameter A_7 characterizes the relative length of the beginning and end of reionization. Park et al. (2013) showed that the model adopted in Battaglia et al. (2013b) failed to account for an asymmetric reionization history and cannot be used to provide universal modeling of the kSZ spectrum. In AMBER, the asymmetry parameter A_7 allows us to have more control over the overall shape of the reionization history and reduce the modeling bias. When we set a large asymmetry, we enforce an earlier but slower beginning, and an earlier and abrupt end of reionization. When $A_z \sim 1$, we get a symmetric reionization history where the beginning and end have equal lengths. In the bottom panels of Figure 7, we show the redshift evolution of n_e and $\Delta T_{\rm kSZ}$ with a symmetric reionization and a highly asymmetric reionization. We can see that even when the duration is kept fixed, for the asymmetric reionization scenario, the ionizing bubbles begin to form at a much earlier redshift.

The right panel of Figure 10 shows the change in the kSZ spectrum when we only change the asymmetry of the reionization history. Compared with the other two reionization history parameters, the dependence of the kSZ spectra on A_z is

weak. We notice that at the $\ell\!=\!3000$ scale where the observation data lie, there is almost complete degeneracy between the different asymmetric reionization cases (but note that the crossover scale may be different for other fiducial parameters). Yet there is a noticeable change in the slope of the kSZ spectrum: a large asymmetry would decrease the power on large scales and introduce slightly more power on small scales. This indicates that to further constrain the early and end phases of reionization in addition to the overall length, we will need more data at multipoles other than $\ell\!=\!3000$.

5.4. Minimum Halo Mass

The minimum halo mass parameter, M_h , is a lower mass limit of halos that host ionizing sources in the simulation. Usually in simulations where we do not keep the reionization history and the photon mean free path fixed, a smaller M_h can lead to earlier reionization because the ionizing sources are more abundant at high redshifts. However, this effect can be counterbalanced if the ionizing photon budget is small (e.g., the escape fraction is low). By directly controlling the reionization history, however, we do not have to explicitly account for the degeneracy between the sources and sinks.

In the left two columns of Figure 11, we show the evolution of the ionization fraction field assuming two extreme values in our parameter study, $M_h = 10^7 M_{\odot}$ and $M_h = 10^{10} M_{\odot}$, while fixing all other parameters at their fiducial values. Because the reionization history is fixed, at each redshift the global ionization fractions are the same. We can see that the change in M_h affects the morphology of ionized regions but not very significantly. Before the universe gets half ionized, larger M_h leads to more large-scale clustering of ionized regions around heavier sources, and there are fewer small ionized regions. In AMBER, when we change M_h from 10^{10} to $10^7 M_{\odot}$, the smaller halos at $z = z_{mid}$ will no longer be treated as sources. However, such effect is small if we only care about the rank ordering of the radiation field; even when the smaller sources are turned on, they will have less radiation compared to large sources, and therefore have a lower priority in reionization compared to larger sources. On the other hand, compared with the nonsource regions, the small sources are likely closer to the large sources than underdense regions are because of the clustering in the structure. Hence, even when smaller sources are not turned on, they are still likely ionized earlier than the underdense regions. We note that one limitation to the above argument is that we currently only use the halo density field at $z_{\rm mid}$ to seed the ionized bubbles. If we instead use a redshiftdependent source field for abundance matching, we may find fewer $M > 10^{10} M_{\odot}$ sources at high redshifts, and so the ionizing bubbles could be more concentrated around larger peaks at the beginning of reionization. In the Appendix, we discuss the effect of abundance matching at various redshifts and show that at the spectrum level the changes due to different abundance matching redshifts are within 5%.

A more quantitative characterization of the difference in clustering is shown in the left and middle panels of Figure 12, where we plot the power spectra of the halo density field and ionization fraction field at $\bar{x}_i = 25\%$, 50% and 75% for two M_h values. From the halo density spectra shown on the left, we see that there is a constant rise in the halo bias by a factor of \sim 3 on large scales, while on scales above $k = 1 \,\mathrm{Mpc}^{-1}h$ the bias increases to >10. The bias contrast in the ionization fraction field, however, is not as significant. On large scales

 $(k < 0.2 \,\mathrm{Mpc}^{-1}h)$, there is a constant increase in power in the $M_h = 10^{10} M_{\odot}$ field but only by <5%. On smaller scales, the power of the $M_h = 10^{10} M_{\odot}$ ionization fraction field falls compared with the $M_h = 10^7 M_{\odot}$ field by ~30% near the end of reionization.

Now that we understand the effect of M_h on the ionization morphology, in the left panel of Figure 13, we show the dependency of D_ℓ^{pkSZ} on M_h , while keeping the reionization history fixed. We can see that, out of all the parameters, M_h has the least effect on the patchy kSZ signal, as should be expected from the small changes in the ionization fraction power spectrum. Only when we limit the sources to be above $10^9\,M_\odot$ can we see a slight increase in the angular power at $\ell \sim 2000$ and suppression of the smaller scale power. This means that a very large M_h can still affect the morphology of ionized regions, even if we fix the reionization history. For smaller M_h values, we do not see an effect on the kSZ spectra when we change M_h . Note that this is not generally true if we do not fix the reionization history, because M_h can affect the timing of reionization and thus the kSZ power.

Figure 13 includes a wide range of M_h from 10^7 to $10^{10} M_{\odot}$. However, the change in D_ℓ^{pkSZ} is at most $0.15~\mu\text{K}^2$ at the higher multipoles. This is in contrast to the result shown in Paul et al. (2021), who predict a $30 \sim 60\%$ increase in $D_{\ell=3000}^{pkSZ}$ with a fixed reionization history. This is likely due to the different assumptions we made in order to keep the reionization history fully controlled (in our case the abundance matching scheme, and in their case, a manually set ionizing efficiency at each time step). In the context of our model, we cannot gain many constraints from D_ℓ^{pkSZ} directly on the ionizing halos. We will need to infer such constraints with extra assumptions on astrophysical parameters that link the reionization history and M_h .

5.5. Radiation Mean Free Path

Finally, we study the mean free path parameter λ_{mfp} that controls on average how far ionizing photons travel in the IGM before being absorbed. Many previous works have empirically related the angular scale at which the patchy kSZ power spectrum reaches its maximum ℓ_{max} to the typical size of ionized regions during reionization (e.g., McQuinn et al. 2005; Iliev et al. 2007; Mesinger et al. 2012; Gorce et al. 2020). Under the scenario described in Section 5.2, larger bubbles result in a larger mean free path, as photons travel through the ionized region without being absorbed. Therefore, the photon mean free path is strongly correlated with the average bubble size during reionization. The ionized bubble size determines the peak of the patchy kSZ spectrum, as we would expect the kSZ spectrum to attain the most power on the scale of the size of these bubbles.

In AMBER, the mean free path parameter $\lambda_{\rm mfp}$ is not equivalent to the physical mean free path of photons measured in the IGM. First, our $\lambda_{\rm mfp}$ is defined at the midpoint of reionization, as opposed to the usual definition at the end of reionization. Second, $\lambda_{\rm mfp}$ does not directly control the size of the ionized regions at a fixed redshift. The sizes of ionized regions depend on the relative radiation intensity as well as the ionization fraction at a specific redshift. Hence, we can imagine that even with $\lambda_{\rm mfp} = 3~{\rm Mpc}~h^{-1}$, the sizes of ionized regions will be much smaller than that at $x_{\rm H~II} = 0.05$. Finally, even though the $\lambda_{\rm mfp}$ is a global parameter, it does not mean that the ionized regions all have fixed sizes. Large halos will still have

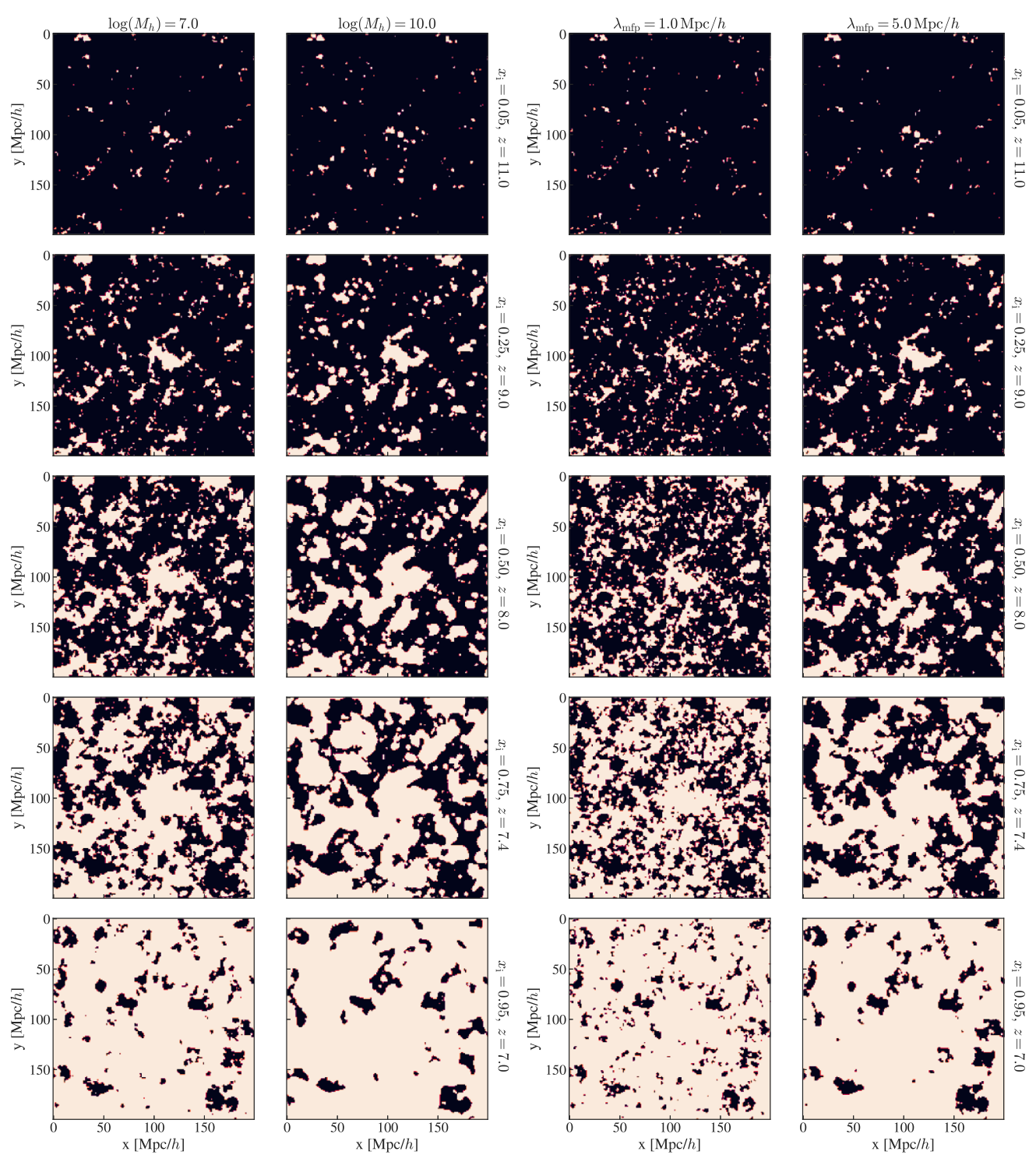


Figure 11. Ionization fraction field across different (mass-weighted) ionization levels, with white regions marking the ionized bubbles. From top to bottom with show a (200 Mpc/h)² × 1 Mpc h^{-1} slice at $\bar{x}_i = 5\%$, 25%, 50%, 75%, and 95%, respectively. Left: ionized regions with a minimum halo mass of $10^7 \, M_\odot$ (first column) and $10^{10} \, M_\odot$ (second column). For a very large minimum halo mass for ionizing galaxies, the ionized bubbles are smoother and more clustered on large scales. However, the overall morphology is not drastically different from when $M_h = 10^7 M_\odot$. Right: ionized regions with $\lambda_{\rm mfp} = 1.0 \, {\rm Mpc} \, h^{-1}$ (third column) and $\lambda_{\rm mfp} = 5.0 \, {\rm Mpc} \, h^{-1}$ (fourth column). We see that in AMBER, for a fixed reionization history, $\lambda_{\rm mfp}$ has a stronger effect on the ionization morphology than the minimum halo mass M_h . For a smaller $\lambda_{\rm mfp}$, the typical sizes of the ionized regions are significantly smaller than for a larger $\lambda_{\rm mfp}$.

larger ionized regions around them, because the photon budget of a cell is affected by the density in addition to the mean free path parameter.

Similar to the previous section, we begin by visualizing the evolution of ionized regions throughout the EoR with various $\lambda_{\rm mfp}$. On the two right columns of Figure 11, we show the

ionization fraction fields for $\lambda_{\rm mfp}=1~{\rm Mpc}~h^{-1}$ and $\lambda_{\rm mfp}=5~{\rm Mpc}~h^{-1}$. Compared to M_h , we see a larger contrast in the ionization morphology when varying $\lambda_{\rm mfp}$: there are more numerous and smaller ionized bubbles in the $\lambda_{\rm mfp}=1~{\rm Mpc}~h^{-1}$ run than in the $\lambda_{\rm mfp}=5~{\rm Mpc}~h^{-1}$ run throughout the entire EoR.

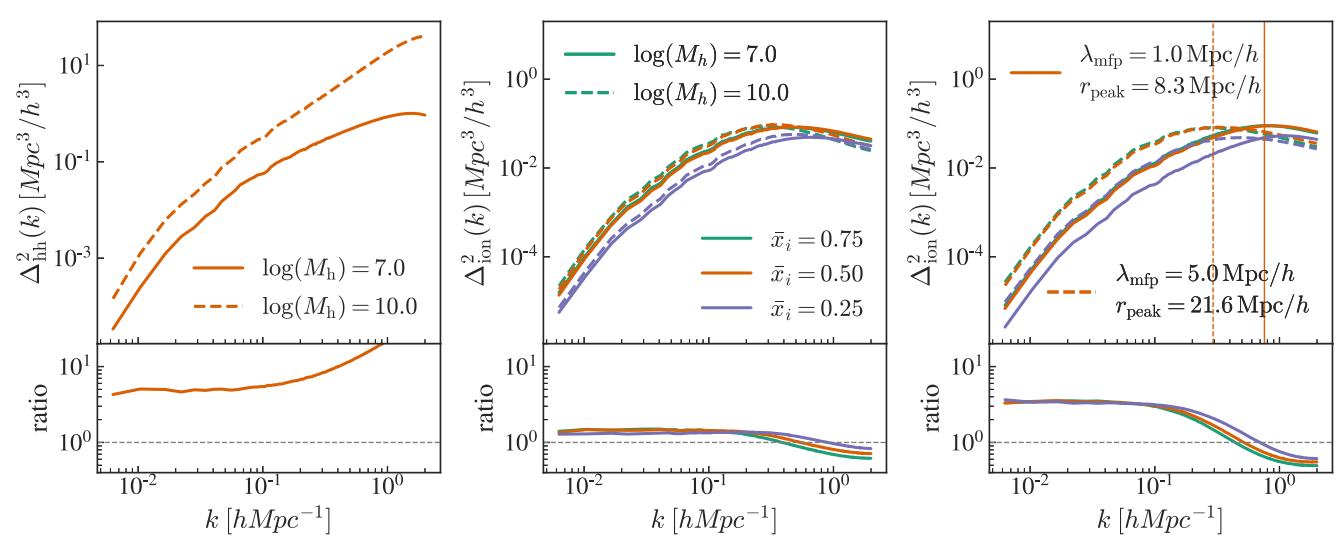


Figure 12. Dimensionless power spectra of the AMBER halo density fields (left) and ionization fraction fields (middle and right) with different minimum halo mass and photon mean free path. For the ionization fraction power spectra we show the spectra at three global ionization levels ($\bar{x}_i = 0.25, 0.50, 0.75$, corresponding to the purple, orange, and green lines, respectively). Left: dimensionless halo density power spectra for $M_h = 10^7 M_{\odot}$ (solid) and $M_h = 10^{10} M_{\odot}$ (dashed). Middle: $\Delta^2_{\rm ion}(k)$ for $M_h = 10^7 M_{\odot}$ (solid) and $M_h = 10^{10} M_{\odot}$ (dashed). Right: $\Delta^2_{\rm ion}(k)$ for $\lambda_{\rm mfp} = 1.0$ Mpc h^{-1} (solid) and $\lambda_{\rm mfp} = 5.0$ Mpc h^{-1} (dashed). The bottom panels show the ratio of the power spectra, with the ratio being $P_{\rm ion,log(M)=10.0}/P_{\rm ion,log(M)=7.0}$ in the left/middle panels and $P_{\rm ion,\lambda=5}/P_{\rm ion,\lambda=1}$ on the right.

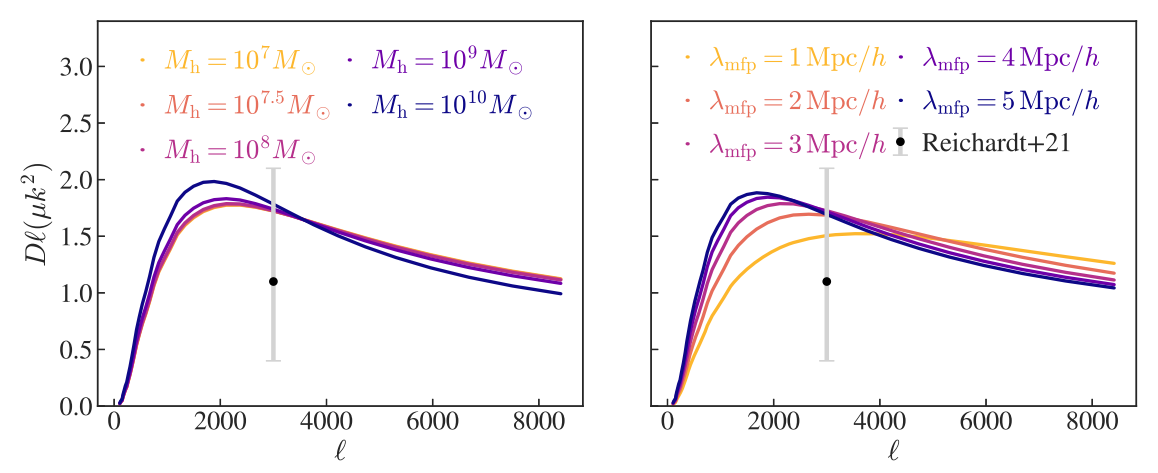


Figure 13. Left: Out of all the parameters, M_h has the least effect on the patchy kSZ signal. Only when we limit the sources to be above $10^9 \, M_\odot$ can we see some suppression on the small-scale power. Right: $\lambda_{\rm mfp}$ is correlated with the average bubble size of ionized bubbles. Increasing the mean free path shifts the peak toward higher multipoles in the kSZ spectrum.

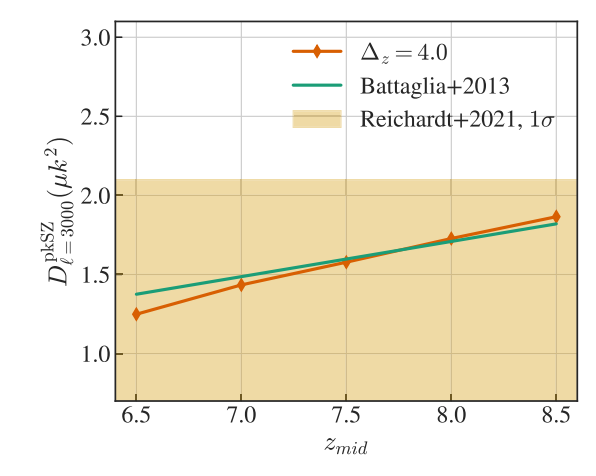
On the right panel of Figure 12, we plot the power spectrum of the ionization fraction field at $\lambda_{mfp} = 1 \text{ Mpc } h^{-1}$ and $\lambda_{\rm mfp} = 5~{\rm Mpc}~h^{-1}$. As was expected from the 2D visualizations, the $\lambda_{\rm mfp} = 5~{\rm Mpc}~h^{-1}$ field has ~ 3 times more power on $k < 0.5~{\rm Mpc}^{-1}h$ scales and half the power on small scales. The increase in $\lambda_{\rm mfp}$ induces an almost-constant large-scale bias at all ionization levels. Compared to M_h , we see that increasing $\lambda_{\rm mfp}$ has a much stronger effect on the ionization morphology. Moreover, there is a shift in the peaking scale of Δ_{ion}^2 with $\lambda_{\rm mfp}$. To correlate the $\lambda_{\rm mfp}$ parameter with the typical sizes of ionized bubbles, we measure the k_{peak} value at which Δ_{ion}^2 peaks, and use $r_{\text{peak}} = 2\pi/k_{\text{peak}}$ to approximate the characteristic size of ionized bubbles. The vertical lines in Figure 12 mark the peaking bubble scales for the ionization fraction 50%. For $\lambda_{\text{mfp}} = 1 \text{ Mpc } h^{-1}$, the characteristic bubble size is $r_{\text{peak}} = 8.3 \text{ Mpc } h^{-1}$. $r_{
m peak} = 8.3 \ {
m Mpc} \ h^{-1}$. $\lambda_{
m mfp} = 5 \ {
m Mpc} \ h^{-1}$ corresponds to $r_{
m peak} = 21.6 \ {
m Mpc} \ h^{-1}$. For more detailed correspondence between $\lambda_{\rm mfp}$ and $r_{\rm peak}$, please refer to the axes of Figure 15.

From the right panel of Figure 13, we see that when we increase the global mean free path of photons, the peak of the

spectrum is shifted toward the higher end of ℓ , corresponding to a larger angular scale subtended by the ionized bubbles. At our fiducial $\lambda_{\rm mfp} = 3.0 \, {\rm Mpc} \, h^{-1}$, the spectrum peaks at $\ell = 2300$. Our finding is consistent with previous works (e.g., Gorce et al. 2020), although our $\lambda_{\rm mfp}$ parameter is different from their characterization of the bubble sizes. We note that our current model has no spatial and temporal variation in $\lambda_{\rm mfp}$. In future works, the halo mass and redshift dependence of $\lambda_{\rm mfp}$ will be studied. The details of where these spectra peak and how they shift with the mean free path will be studied later in Section 5.6.

5.6. Scaling of $D_{\ell=3000}^{pkSZ}$ with the Reionization Parameters

As was discussed in the previous sections, the amplitude of the kSZ spectrum is most sensitive to $z_{\rm mid}$ and Δ_z , the slope of the spectra is affected by A_z , and the peak of the kSZ spectrum is most sensitive to $\lambda_{\rm mfp}$. Now we want to study more quantitatively the dependence of the amplitude and shape of the kSZ spectrum on the reionization parameters. Note that, for the



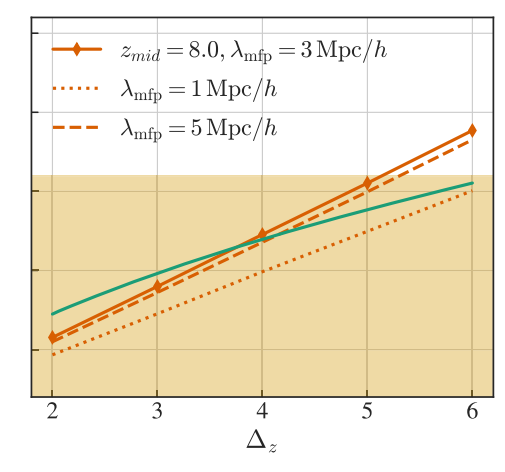


Figure 14. Relationship between the amplitude of the kSZ angular power spectra D_ℓ^{pkSZ} at $\ell=3000$ and the redshift and duration of reionization. The yellow regions are the 1σ constraint from Reichardt et al. (2021). Left: For a fixed duration $\Delta_z=4.0$, AMBER produces D_ℓ^{pkSZ} , which scales almost linearly with the midpoint redshift of reionization (orange). Compared with the scaling relation fitted in Battaglia et al. (2013a; green), we have a slightly steeper slope. Right: When we fix $z_{\text{mid}}=8.0$, D_ℓ^{pkSZ} also scales linearly with the duration of reionization. Compared with Battaglia et al. (2013a) who found a power-law dependence of ~ 0.47 , we find a steeper dependence of D_ℓ^{pkSZ} and D_ℓ^{pkSZ} are dependence of the scaling relation on D_ℓ^{pkSZ} and D_ℓ^{pkSZ} are dependence of the scaling relation on D_ℓ^{pkSZ} and D_ℓ^{pkSZ} are dependence of the scaling relation on D_ℓ^{pkSZ} and D_ℓ^{pkSZ} and D_ℓ^{pkSZ} are dependence of the scaling relation on D_ℓ^{pkSZ} and D_ℓ^{pkSZ} are dependence of the scaling relation on D_ℓ^{pkSZ} and D_ℓ^{pkSZ} are dependence of the scaling relation on D_ℓ^{pkSZ} and D_ℓ^{pkSZ} are dependence of the scaling relation on D_ℓ^{pkSZ} and D_ℓ^{pkSZ} are dependence of the scaling relation on D_ℓ^{pkSZ} and D_ℓ^{pkSZ} are dependence of the scaling relation on D_ℓ^{pkSZ} and D_ℓ^{pkSZ} are dependence of the scaling relation on D_ℓ^{pkSZ} and D_ℓ^{pkSZ} are dependence of the scaling relation of D_ℓ^{pkSZ} and D_ℓ^{pkSZ} are dependence of the scaling relation of D_ℓ^{pkSZ} and D_ℓ^{pkSZ} are dependence of the scaling relation of D_ℓ^{pkSZ} and D_ℓ^{pkSZ} are dependence of

scaling relation study, we always only change one parameter at a time and keep the other parameters fixed at their fiducial values.

In Figure 14, we show the amplitude of kSZ at $\ell=3000$ with different $z_{\rm mid}$ and Δ_z values, respectively. From both panels, $D_{\ell=3000}^{\rm pkSZ}$ scales almost linearly with the parameter values. For comparison, we also plotted the scaling relation fitted in Battaglia et al. (2013a; Equation (10) in their paper). Note that in Battaglia et al. (2013a), the duration is defined to be $\Delta_{z,50}$, and the asymmetry parameter is not measured. For comparison with our Δ_z , we assume an asymmetry of $A_z=3$ and use the Weibull function (Equation (10)) to specify the reionization history at $\Delta_z=[2, 3, 4, 5, 6]$. Then, for each of these reionization histories, we measure the value of $\Delta_{z,50}$. Finally, we input these measured $\Delta_{z,50}$ values into the Battaglia et al. (2013a) fits together with a specified $z_{\rm mid}$ value to obtain the green lines.

Comparing with Battaglia et al. (2013a)'s power-law index of 0.47 on the duration, our measured $D_{\ell=3000}^{\text{pkSZ}}$ has a steeper dependence on Δ_z . This is consistent with the findings of Gorce et al. (2020), although we did not directly show their results as we have different z_{mid} values. One possible difference in the scaling is the asymmetrical nature of our reionization histories. As was shown in Figure 1, if the asymmetry of the reionization history is not fixed, the relation between $\Delta_{z,50}$ and $\Delta_{z,90}$ may not be linear. Thus Battaglia et al. (2013a)'s 0.47 power-law index could result from an increase in asymmetry with the duration under their model. Another possible explanation is that Battaglia et al. (2013a) does not independently control the mean free path parameter, which degenerates with Δ_z at the latest are particled, which degenerates with Δ_z at $\ell=3000$. To demonstrate the effect of $\lambda_{\rm mfp}$ on the Δ_z dependency, on the right panel we show the $D_{\ell=3000}^{\rm pkSZ} - \Delta_z$ relation for $\lambda_{\rm mfp}=1~{\rm Mpc}~h^{-1}$ and $\lambda_{\rm mfp}=5~{\rm Mpc}~h^{-1}$. We see that $D_{\ell=3000}^{\rm pkSZ}$ actually peaks around $\lambda_{\rm mfp}=3~{\rm Mpc}~h^{-1}$, and the values at $\lambda_{\rm mfp}=1~{\rm Mpc}~h^{-1}$ and $\lambda_{\rm mfp}=5~{\rm Mpc}~h^{-1}$ are both lower. In the Battaglia et al. (2013a) model, because there is a lower. In the Battaglia et al. (2013a) model, because there is a decrease in λ_{mfp} with increased duration (see, e.g., Figure 9 of Battaglia et al. 2013b) as the large-scale bias parameter of the reionization-redshift field is fixed (e.g., Trac et al. 2021), the $D_{\ell=3000}^{\text{pkSZ}} - \Delta_z$ relation deviates from a linear relationship.

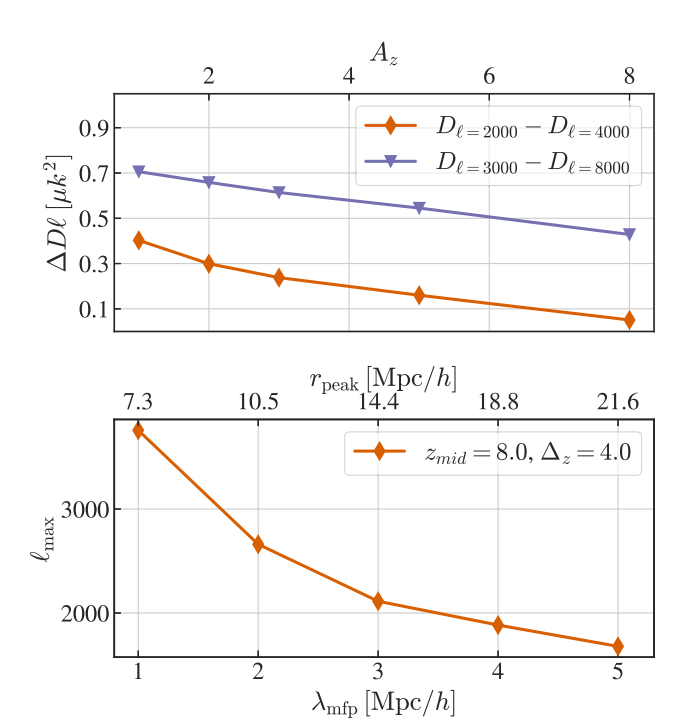


Figure 15. Top: Change in the slope of the kSZ power spectrum with the asymmetry of the reionization history A_z . Here we show the difference between two sets of ℓ values: $D_{\ell=2000}-D_{\ell=4000}$ (orange), which is close to the current measurement at $\ell=3000$, and $D_{\ell=3000}-D_{\ell=8000}$ (purple), which requires an extra measurement at a relatively high ℓ . Bottom: shift in the peak of kSZ spectrum with the mean free path parameter $\lambda_{\rm mfp}$ (bottom axis) and the mean bubble size (top axis).

Next, we look at how the asymmetry of reionization and $\lambda_{\rm mfp}$ affect different aspects of the kSZ spectrum. In the top panel of Figure 15, we plot the difference between the amplitudes at two sets of multipoles as a function of A_z . We show $D_{\ell=2000}-D_{\ell=4000}$, which is close to the current measurement at $\ell=3000$, and $D_{\ell=3000}-D_{\ell=8000}$, which requires an extra measurement at a relatively high value of $\ell=8000$. As we have discussed in Section 5.3, the spectra get flatter as asymmetry rises, and so $\Delta D_{\ell}^{\rm pkSZ}$ falls with larger A_z . The difference between $D_{\ell=3000}$ and $D_{\ell=8000}$ is larger at all A_z

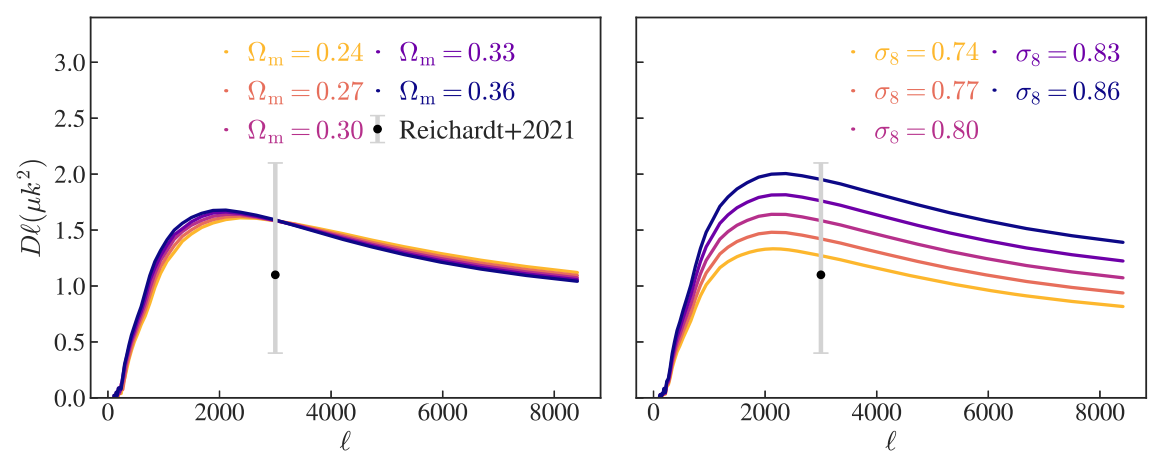


Figure 16. Patchy kSZ angular power spectrum with the same reionization history but different cosmological parameters (Ω_m and σ_8). While there is complete degeneracy between different Ω_m values at $\ell = 3000$, σ_8 affects the kSZ amplitude on all scales.

values, but the constraining power on A_z is similar between the two sets of ΔD_ℓ s. To distinguish between two asymmetry values such as $A_z=1$ and $A_z=8$, we need to be able to measure either $D_{\ell=2000}-D_{\ell=4000}$ or $D_{\ell=3000}-D_{\ell=8000}$ at $\sim 0.3~\mu$ k² accuracy. Previously, Gorce et al. (2020) argued that focusing on $D_{\ell=3000}$ is not sufficient for characterizing the kSZ signal, especially with various reionization scenarios that lead to asymmetric reionization histories. Our result further supports this argument by showing a quantitative scaling between the slope of the kSZ power and the asymmetry of reionization.

In the bottom panel of Figure 15, we plot the location of the kSZ power spectrum peaks as a function of $\lambda_{\rm mfp}$. From the plot we see that $\ell_{\rm max}$ scales as $1/\lambda_{\rm mfp}$. This is expected as $\lambda_{\rm mfp}$ is correlated with the size of the ionized regions and is in general agreement with Figure 9 of Gorce et al. (2020). To establish a correspondence between our effective mean free path parameter and the typical ionized bubble size at $z_{\rm mid}$, on the top axis we label the peaking scale of the ionizing-fraction power spectrum (i.e., the right panel of Figure 12). At our fiducial $\lambda_{\rm mfp} = 3~{\rm Mpc}~h^{-1}$, the typical bubble size is 14.4 Mpc h^{-1} (comoving) at z=8.

We note that for all the scaling relations shown in this section, we always fix all other reionization parameters and vary them one at a time. This means that all the relations are conditioned, and so one should take caution when using such scaling relations directly to perform parameter constraints.

5.7. Cosmological Parameters

The process of reionization involves a complicated interplay between cosmological and astrophysical parameters, a large fraction of which remain highly uncertain. For instance, a larger σ_8 could lead to earlier onset of reionization, provided that the nature of the ionizing sources and the photon escape fraction are fixed. However, there is a lack of comprehensive studies on how different cosmologies affect the astrophysics of reionization. In AMBER, the reionization history and cosmology are modeled independently. This circumvents the complicated treatment and unknown relation between the two, and allows us to separately analyze the effect of cosmology on the patchy kSZ signal. In this section, we study the change in the kSZ power spectra when we change two cosmological parameters, $\Omega_{\rm m}$ and σ_8 .

In Figure 16, we show the change in the patchy kSZ spectra when we vary Ω_m and σ_8 . From the left panel, we can see that

 D_{ℓ}^{pkSZ} is only weakly sensitive to the change in Ω_m , especially at $\ell = 3000$. Larger Ω_m leads to slightly higher amplitudes on ℓ < 2000 scales. On the right panel, σ_8 has a more direct effect on the amplitude of the kSZ spectrum; the kSZ power doubles when we change σ_8 from 0.74 to 0.86. Such effect comes from two different sources. First, in linear theory, both the density and velocity fluctuations scale as σ_8^2 . As the kSZ effect measures the momentum fluctuations, we should expect a $\sim \sigma_{x}^{4}$ contribution from the change in the matter density and velocity fields (see also, e.g., Trac et al. 2011; Shaw et al. 2012). Second, the change in density contrast and clustering can also influence the reionization-redshift field through the radiation intensity. Hence, a change in σ_8 will also affect the morphology of ionized regions at different redshifts. By comparing with the effects of reionization parameters in Figures 10 and 13, we see that there are degeneracies between σ_8 , Δ_z , $z_{\rm mid}$, and $\lambda_{\rm mfp}$ in terms of $D_{\ell=3000}^{\text{pkSZ}}$.

Compared with reionization parameters such as z_{mid} and Δz , which only affect the patchy kSZ and τ_e through the reionization redshifts, cosmological parameters change the signals through both the density/velocity fields and the reionization-redshift field (which is also correlated with the change in the density). For example, when we change σ_8 from 0.8 to 0.7, the decrease in the matter power spectrum will in itself reduce $P_{ee}(k)$, even when the reionization redshift and morphology are fixed. On the other hand, decreasing the amplitude of the matter power spectrum also results in a different reionization-redshift field, as the number of large ionizing sources decreases at the midpoint of reionization. In order to disentangle the change due to matter density from the change due to the reionization-redshift field when varying σ_8 , we show in Figure 17 the change in $P_{ee}(k, z)$ purely from z_{re} , compared with the total change, at different ionization levels. Here we compare the ratio between $P_{ee}(k, z)$ at $\sigma_8 = 0.74$ with $P_{ee}(k, z)$ at the fiducial value $\sigma_8 = 0.8$. For the dashed curve, we simply change the value of σ_8 in the code, so that both the gas density and the reionization-redshift fields are affected. For the solid curve, we use $\sigma_8 = 0.74$ to generate the reionizationredshift field, while the matter overdensity is kept at $\sigma_8 = 0.8$. By comparing the dashed curves at different ionization levels, we see that, as the ionization level \bar{x}_i increases, the ratio between the two P_{ee} ratios drops on all scales. Noticeably, only near the end of reionization at $\bar{x}_i = 0.95$ does the P_{ee} ratio approach the expected matter power spectrum ratio of 0.85 on

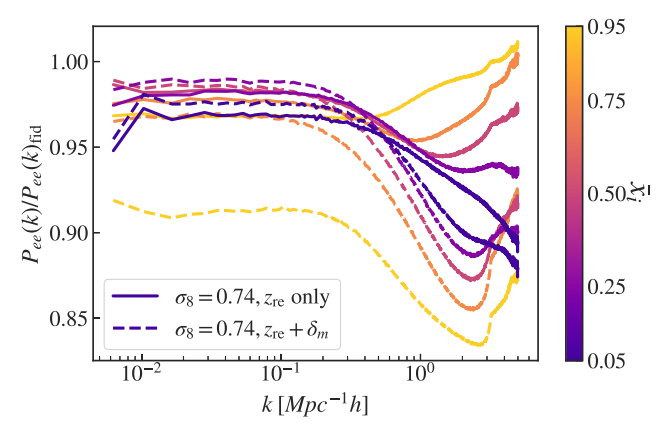


Figure 17. Ratio between the electron number density power spectra $P_{ee}(k)$ at $\sigma_8=0.74$ and $\sigma_8=0.8$ (the fiducial value). The solid curves are generated by changing only the reionization-redshift field $z_{\rm re}$ to $\sigma_8=0.74$, while the dashed curves are generated by changing both $z_{\rm re}$ and the matter density field δ_m . The different colors represent the spectra at different ionization levels.

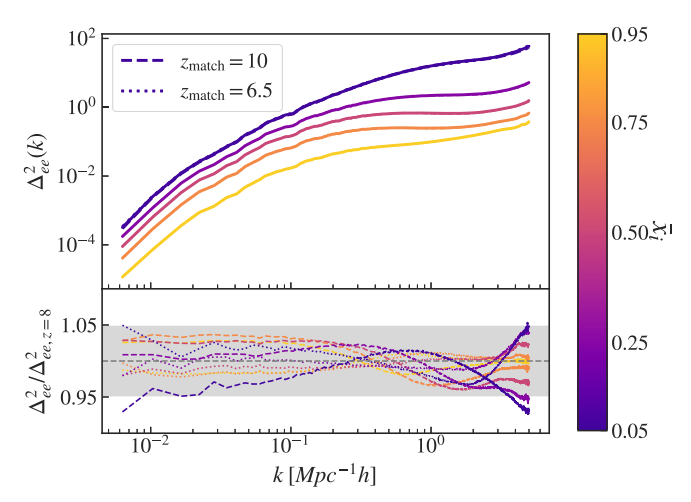
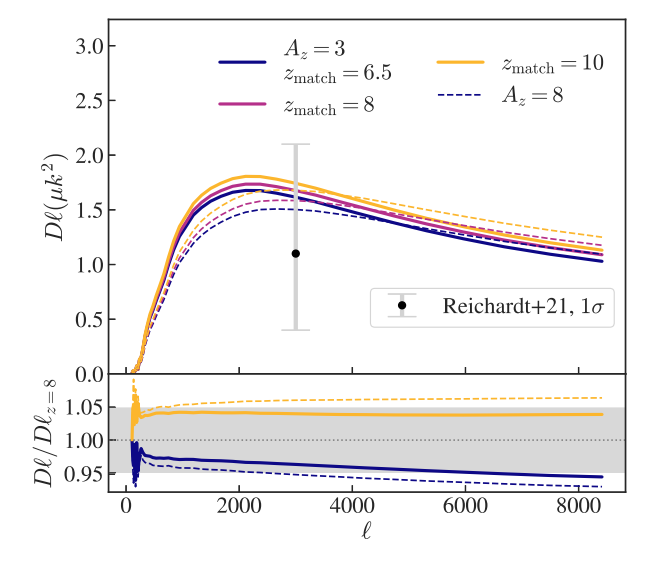


Figure A1. Free-electron number density power spectra at different stages of reionization, calculated based on reionization-redshift fields matched at $z_{\rm match}=8$ (solid), $z_{\rm match}=10$ (dashed), and $z_{\rm match}=6.5$ (dotted). The bottom panel shows the ratio between the $\Delta_{\rm ee}^2$ at $z_{\rm match}=10$ ($z_{\rm match}=6.5$) and that at the fiducial $z_{\rm match}=z_{\rm mid}=8$.

large scales. At higher ionization levels, the effect of the matter density field is subdominant, especially on large scales, where >95% of the power is retained. On small scales $(k>1~{\rm Mpc}~h^{-1})$, however, the power drops significantly. By comparing with the solid curves where only $z_{\rm re}$ varies, we can see that the suppression on small scales still comes from the change in δ_m instead of $z_{\rm re}$, as the suppression in the solid curves is not as significant. Therefore, we conclude that changing σ_8 mostly affects P_{ee} near the end of reionization. Before the end of reionization, the change in $z_{\rm re}$ has a dominant effect over δ_m on large scales and only mildly affects P_{ee} . On small scales, P_{ee} is mainly affected by the matter density and varies more significantly with σ_8 .

6. Conclusion

In this work, we use the new semi-numerical code for reionization AMBER to study the patchy kSZ effect under different reionization scenarios. We calibrate and test the AMBER predictions against the radiative-transfer RadHydro simulation suite (Doussot et al. 2019). We find that, at our target resolution of 1 Mpc h^{-1} , AMBER produces an electron



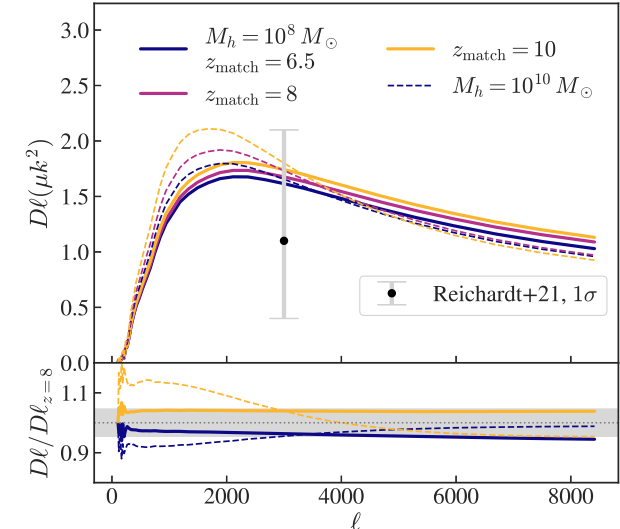


Figure A2. Patchy kSZ power spectra calculated for a reionization-redshift field that is abundance matched at different points across the reionization history. Here we have always assumed fiducial values of $z_{\rm mid}=8$ and $\Delta_z=4$, but the z_{re} fields are abundance matched against the radiation field at $z_{\rm match}=6.5$ (dark blue), $z_{\rm match}=8$ (purple), and $z_{\rm match}=10$ (yellow). Top: effect of $z_{\rm match}$ at the fiducial value $A_z=3$ as well as a larger asymmetry of $A_z=8$. Bottom: effect of $z_{\rm match}$ at the fiducial value $M_h=10^8\,M_\odot$ and a larger source threshold of $M_h=10^{10}\,M_\odot$.

number density field and kSZ angular power spectra that resemble those from RadHydro at all redshifts.

AMBER explicitly parameterizes the reionization history by the midpoint redshift, duration, and asymmetry parameters. By varying the midpoint redshift of reionization, we find that the range $z_{\rm mid} = [6.0,~8.9]$ has Thomson optical depth values consistent with the Planck Collaboration et al. (2020) measurements at the 2σ level. We also find that the peaking scale of the kSZ angular power spectrum is not sensitive to the midpoint redshift.

Then, assuming a value of $z_{\rm mid}=8.0$, consistent with the Planck measurement, and fixing the other parameters at their fiducial values, we find that the amplitude of $D_\ell^{\rm pkSZ}$ at $\ell=3000$ scales linearly with the duration of reionization Δ_z . The resulting $D_{\ell=3000}^{\rm pkSZ}$ values are consistent with the 1σ measurement from Reichardt et al. (2021) up to $\Delta_z < 5.1$ (Δ_z here encloses redshifts from 5% to 95% reionization). This

translates to $\Delta_{z,50} < 2.0$ under the definition of duration in Battaglia et al. (2013b), assuming a mildly asymmetric reionization history at $A_z = 3$. Then, allowing for other reionization parameters to vary simultaneously, we find that $\Delta_z < 12.8$ is the maximum duration consistent with the Reichardt et al. (2021) estimation at the 2σ level ($\Delta_{z,50} < 3.5$ assuming $A_z = 8$). Note that this extreme scenario requires a high asymmetry of the reionization history of $A_z > 8$ in order for reionization to end before z = 5.5. This is in broad agreement with the constraint from Reichardt et al. (2021) of $\Delta_{z,50} < 5.4$ (95% CL) using the Battaglia et al. (2013a) model and the constraint by Choudhury et al. (2021) at $\Delta_{z,50} < 2.9$ (99% CL) using a different semi-numerical model.

Then, by considering reionization histories with different degrees of asymmetry, we find that the kSZ amplitude at $\ell=3000$ is not sensitive to the detailed shape of the reionization history beyond the redshift and duration. However, the slope of the kSZ angular power spectrum does depend on the asymmetry. This is in line with the results shown in, for example, Park et al. 2013 and Gorce et al. 2020 and makes constraints on the beginning and end of reionization through patchy kSZ possible if measurements are made at different multipoles. Nevertheless, we find that constraints on the asymmetry require $\sim 0.1 \, \mu k^2$ measurement accuracy of the patchy kSZ power spectrum at various multipoles other than $\ell=3000$.

We also independently control the size of sources through the minimum halo mass (M_h) and the relative radiation intensity through the effective mean free path ($\lambda_{\rm mfp}$). With a fixed reionization history, the minimum halo mass has little effect on the ionization morphology at a fixed redshift. Therefore, the amplitude and shape of the kSZ spectrum are only mildly affected by the minimum halo mass M_h . This is in contrast to the results shown in Paul et al. (2021), and thus a more detailed investigation regarding which assumptions in our models lead to the differences is needed. The effective photon mean free path affects the peaking location of the kSZ power spectrum, and at our fiducial $\lambda_{\rm mfp} = 3 \,{\rm Mpc} \, h^{-1}$ (fitted to the RadHydro simulations) the spectrum peaks at $\ell \approx 2100$. Moreover, we explicitly showed that there is a degeneracy between the mean free path $\lambda_{\rm mfp}$ and the duration of reionization in terms of $D_\ell^{\rm pkSZ}$ at $\ell=3000$. A shorter $\lambda_{\rm mfp}$ can lead to a ${\sim}10\%$ lower $D_{\ell=3000}^{\rm pkSZ}$ and a flatter slope in the $D_{\ell=3000}^{
m pkSZ} - \Delta_z$ scaling relation. This partly explains the steeper power-law scaling relationship we get compared with Battaglia et al. (2013a), as the ionized bubble sizes in their model decrease with longer duration.

Finally, we study the effect of cosmological parameters Ω_m and σ_8 on the patchy kSZ power spectrum under fixed reionization parameters. We find that with a fixed reionization history, the kSZ power spectrum does not undergo noticeable changes with Ω_m , especially near $\ell=3000$. However, σ_8 affects the overall amplitude of the kSZ power spectrum, which results in a degeneracy between σ_8 and Δ_z . On large scales $(k<1~{\rm Mpc}^{-1}h)$, σ_8 affects the electron number density mainly through the $z_{\rm re}$ field, while on small scales $(k<1~{\rm Mpc}^{-1}h)$ the effect comes from the matter density field.

Even though we have provided a rough estimate of the duration of reionization consistent with current observations from ground-based telescopes, such constraints are only a first-order estimation because we only search a 1D parameter space at a time. To carry out the analysis properly, we need to take

into account the correlation between different parameters by marginalizing over other model parameters. In order to achieve that, we will need a tool to estimate the kSZ spectra faster than what we can achieve with our simulations.

Moreover, in order to separate out the patchy component from the spectrum, one would need a good description of the homogeneous spectrum. Currently, the homogeneous spectrum quoted in Reichardt et al. (2021) comes from Shaw et al. (2012), but we can use results updated with more recent simulations (e.g., He et al. 2022) to get a better estimation of how accurately one can recover the patchy signal.

We thank Marcelo Alvarez and Matthew McQuinn for reading the manuscript and providing important comments and suggestions. H.T. acknowledges support from the NSF AI Institute: Planning: Physics of the Future, NSF PHY2020295. The simulations were run on the Vera and Bridges-2 clusters at the Pittsburgh the Supercomputing Center.

Appendix Effect of Abundance Matching at the Midpoint Redshift

In Section 3.1.2, we mentioned that, currently in AMBER, the reionization-redshift field is abundance matched against the radiation intensity at a single redshift $z_{\rm mid}$ for computation efficiency. However, we do note that due to the nonlinear growth of structure and especially the nonlinearity in the halo density field, this choice can cause uncertainties in the EoR observables. To make the model more physical, we will work toward a tomographic abundance matching scheme, where the reionization redshift is determined by the source field at several redshifts spanning the EoR. As this work is based on single-redshift abundance matching, here we characterize the level of uncertainties induced by the choice of the abundance matching redshift $z_{\rm match}$.

We keep all parameters at their fiducial values unless otherwise stated (in particular, we always fix $z_{mid} = 8$), and we change the redshift at which we generate the source field for matching $z_{re}(x)$. Here we have chosen two relatively extreme values: at z = 10, $x_{\rm H~II} \approx 0.1$ and reionization has just started; at z = 6.5, $x_{\rm H~II} \approx 0.95$ and we are approaching the end of EoR. We note that for single-redshift abundance matching, $z_{\text{match}} = z_{\text{mid}}$ is still a better choice than others. At higher redshifts, the sources are scarce, and so the resulting $z_{re}(x)$ can be noisier. The sources at lower redshifts are more abundant, but they are not the main driver of reionization as the EoR has almost finished by then. Hence, the $z_{\rm mid}$ halos are a better representation of the sources that are responsible for driving the ionization process. Here by showing the z_{match} at extreme values, we aim to bracket the range of uncertainty caused by the single-redshift abundance matching.

In Figure A1, we show the (dimensionless) free-electron number density power spectra Δ^2_{ee} with $z_{\rm re}(x)$ matched against the radiation field at $z_{\rm match}=6.5$, $z_{\rm match}=8$ (which corresponds to $z_{\rm mid}$), and $z_{\rm match}=10$. Compared with the original choice of $z_{\rm match}=8$, using the source field at $z_{\rm match}=10$ increases the power on most scales by a constant factor of <5% except at the beginning of reionization, and there is a larger difference on small scales than on large scales. Using the reionization redshift matched at a later time ($z_{\rm match}=6.5$) reduces Δ^2_{ee} by <5%.

Figure A2 shows the effect of changing $z_{\rm match}$ on the patchy kSZ power spectra. At our fiducial set of reionization parameters (see Table 2), using $z_{\rm match} = 10$ increases the kSZ

power at $\ell > 1000$ by an almost-constant factor of 5%, while using $z_{\text{match}} = 6.5$ reduces the power by a similar fraction (shown by the solid curves on both the top and bottom plots). To further investigate the potentially larger influence of z_{match} on highly asymmetric reionization scenarios, we also show on the top panel the difference between three z_{match} values at A_z = 8 (without changing the midpoint or the duration). We see that, for a larger A_z , the change in D_ℓ is indeed larger, but the overall fluctuation is still kept within $\sim 7\%$ on all scales of interest. On the bottom panel of Figure A2, we show the effect of various z_{match} values for larger sources at $M_h = 10^{10} M_{\odot}$. A higher source threshold is expected to enlarge the effect of varying z_{match} , as the halo mass function increases more with the redshift at the high-mass end. Indeed, we can see that, for $M_h = 10^{10} M_{\odot}$, the deviation of $z_{\text{match}} = 10$ and $z_{\text{match}} = 6.5$ from $z_{\text{match}} = 8$ reaches a maximum of $\sim 15\%$ at $\ell = 500-1000$. Nonetheless, on the scale of interest for the patchy kSZ measurement ($\ell \gtrsim 2000$), the effect of z_{match} is still kept within 5%. Hence, we conclude with our investigations that changing the redshift at which we match the reionization-redshift field does have an impact at the observable level, but on the scale of interest this impact is within \sim 5%.

ORCID iDs

Nianyi Chen https://orcid.org/0000-0001-6627-2533 Hy Trac https://orcid.org/0000-0001-6778-3861 Renyue Cen https://orcid.org/0000-0001-8531-9536

References

```
Addison, G. E., Dunkley, J., & Bond, J. R. 2013, MNRAS, 436, 1896
Alvarez, M. A. 2016, ApJ, 824, 118
Alvarez, M. A., Ferraro, S., Hill, J. C., Hložek, R., & Ikape, M. 2021, PhRvD, 103, 063518
Battaglia, N., Natarajan, A., Trac, H., Cen, R., & Loeb, A. 2013a, ApJ, 776, 83
Battaglia, N., Trac, H., Cen, R., & Loeb, A. 2013b, ApJ, 776, 81
Becker, G. D., Bolton, J. S., Madau, P., et al. 2015, MNRAS, 447, 3402
Bond, J. R., Cole, S., Efstathiou, G., & Kaiser, N. 1991, ApJ, 379, 440
Bouwens, R. J., Illingworth, G. D., Oesch, P. A., et al. 2015, ApJ, 803, 34
Carlstrom, J. E., Holder, G. P., & Reese, E. D. 2002, ARA&A, 40, 643
Chen, N., Doussot, A., Trac, H., & Cen, R. 2020, ApJ, 905, 132
Choudhury, T. R., Mukherjee, S., & Paul, S. 2021, MNRAS, 501, L7
```

```
de Belsunce, R., Gratton, S., Coulton, W., & Efstathiou, G. 2021, MNRAS,
  507, 1072
DeBoer, D. R., Parsons, A. R., Aguirre, J. E., et al. 2017, PASP, 129, 045001
Doussot, A., Trac, H., & Cen, R. 2019, ApJ, 870, 18
Dunkley, J., Calabrese, E., Sievers, J., et al. 2013, JCAP, 2013, 025
Ferraro, S., & Smith, K. M. 2018, PhRvD, 98, 123519
Finkelstein, S. L., Ryan, R. E., Jr., Papovich, C., et al. 2015, ApJ, 810, 71
Furlanetto, S. R., Zaldarriaga, M., & Hernquist, L. 2004, ApJ, 613, 1
George, E. M., Reichardt, C. L., Aird, K. A., et al. 2015, ApJ, 799, 177
Glazer, D., Rau, M. M., & Trac, H. 2018, RNAAS, 2, 135
Gorce, A., Ilić, S., Douspis, M., Aubert, D., & Langer, M. 2020, A&A,
  640, A90
Górski, K. M., Hivon, E., Banday, A. J., et al. 2005, ApJ, 622, 759
He, Y., Trac, H., & Gnedin, N. Y. 2022, ApJ, 925, 134
Iliev, I. T., Pen, U.-L., Bond, J. R., Mellema, G., & Shapiro, P. R. 2007, ApJ,
  660, 933
Keating, L. C., Weinberger, L. H., Kulkarni, G., et al. 2020, MNRAS,
  491, 1736
Koopmans, L., Pritchard, J., Mellema, G., et al. 2015, in Advancing
   Astrophysics with the Square Kilometre Array (AASKA14) (Trieste: PoS)
McQuinn, M., Furlanetto, S. R., Hernquist, L., Zahn, O., & Zaldarriaga, M.
  2005, ApJ, 630, 643
Mesinger, A., Furlanetto, S., & Cen, R. 2011, MNRAS, 411, 955
Mesinger, A., McQuinn, M., & Spergel, D. N. 2012, MNRAS, 422, 1403
Ostriker, J. P., & Vishniac, E. T. 1986, ApJL, 306, L51
Pagano, L., Delouis, J. M., Mottet, S., Puget, J. L., & Vibert, L. 2020, A&A,
Park, H., Shapiro, P. R., Komatsu, E., et al. 2013, ApJ, 769, 93
Paul, S., Mukherjee, S., & Choudhury, T. R. 2021, MNRAS, 500, 232
Planck Collaboration, Aghanim, N., Akrami, Y., et al. 2020, A&A, 641, A6
Reichardt, C. L., Patil, S., Ade, P. A. R., et al. 2021, ApJ, 908, 199
Shaw, L. D., Rudd, D. H., & Nagai, D. 2012, ApJ, 756, 15
Smith, K. M., & Ferraro, S. 2017, PhRvL, 119, 021301
Spergel, D., Gehrels, N., Baltay, C., et al. 2015, arXiv:1503.03757
Sunyaev, R. A., & Zeldovich, I. B. 1980, ARA&A, 18, 537
Tashiro, H., Aghanim, N., Langer, M., et al. 2011, MNRAS, 414, 3424
Trac, H., Bode, P., & Ostriker, J. P. 2011, ApJ, 727, 94
Trac, H., Cen, R., & Loeb, A. 2008, ApJL, 689, L81
Trac, H., Cen, R., & Mansfield, P. 2015, ApJ, 813, 54
Trac, H., Chen, N., Holst, I., Alvarez, M. A., & Cen, R. 2021, ApJ, 927, 186
Weibull, W. 1951, JAM, 18, 293
Windhorst, R. A., Cohen, S. H., Jansen, R. A., Conselice, C., & Yan, H. 2006,
       VAR. 50, 113
Zahn, O., Lidz, A., McQuinn, M., et al. 2007, ApJ, 654, 12
Zahn, O., Mesinger, A., McQuinn, M., et al. 2011, MNRAS, 414, 727
Zahn, O., Reichardt, C. L., Shaw, L., et al. 2012, ApJ, 756, 65
Zeldovich, Y. B., & Sunyaev, R. A. 1969, Ap&SS, 4, 301
Zhang, P., Pen, U.-L., & Trac, H. 2004, MNRAS, 347, 1224
```